

Faculty of Physics and Astrophysics

Ruperto-Carola University of Heidelberg

Diplomathesis in Physics

submitted by

Isabelle Karina Wenig

born in Brussels

2008

Statistical correlation studies of astrophysical objects with H.E.S.S. data

This diploma thesis has been carried out by Isabelle K. Wenig

Max Planck Institute for Nuclear Physics

under the supervision of

Prof. W. Hofmann

Max Planck Institute for Nuclear Physics

Kurzfassung: In den letzten Jahren haben die technischen Fortschritte in der Hoch-Energie Gamma Astronomie die Entdeckung vieler neuen Quellen ermöglicht. Die meisten dieser Quellen wurden mit dem H.E.S.S. Experiment, einem System von vier abbildenden Cherenkov-Teleskopen in Namibia, entdeckt. Ein Großteil der Quellen werden als Pulsarwindnebel identifiziert, es werden jedoch auch Supernova-Überreste und massive Röntgendoppelsterne detektiert. Dennoch bleiben viele Quellen ohne klar identifizierbaren Ursprung.

In dieser Arbeit wird eine Studie vorgestellt, welche, im Gegensatz zu der Suche nach einzelnen Übereinstimmungen, statistische Korrelationen zwischen unterschiedlichen astrophysikalischen Objekten und den H.E.S.S. Quellen in der Galaktischen Ebene untersucht. Die Ergebnisse zeigen, dass HII Regionen, OB Sterne und Galaktische Blasen nicht mit hoch-energetischen γ -Strahlen korrelieren, während die erwartete Korrelationen mit Supernova-Überresten und massiven Röntgendoppelsternen unter der geringen Statistik der Daten leiden. Pulsarwindnebel sowie Sternentstehungsgebiete und -komplexe scheinen mit hoch-energetischen γ -Strahlen korreliert zu sein.

Abstract: Recent advances in the instrumentation to observe very high energy (VHE) gamma rays have made the discovery of many new sources possible, most of them being discovered in the Galactic plane survey of H.E.S.S., an array of imaging atmospheric Cherenkov telescopes in Namibia. Of these sources, a significant number can be identified as pulsar wind nebulae, but supernova remnants and high mass X-ray binaries were also detected. However, a large fraction of the sources remains with no clear counterpart.

In this work a study is presented searching for statistical correlations between different types of astrophysical objects and all the H.E.S.S. sources in the Galactic plane, rather than looking for counterparts for individual sources. The results of this work show that HII regions, OB stars and Galactic bubbles do not correlate significantly with VHE γ -ray sources, while the expected correlations with supernova remnants and high mass X-ray binaries are limited due to the low statistics. Pulsar wind nebulae, regions of star formation and star forming complexes seem to correlate with VHE γ -ray sources.

Contents

1	Introduction	1
2	Gamma ray astronomy with H.E.S.S.	5
2.1	The physics of very high energy γ -rays	5
2.1.1	Production mechanisms of γ -rays	5
2.1.2	Acceleration mechanisms of charged particles	6
2.2	The H.E.S.S. experiment	9
2.2.1	Air showers	9
2.2.2	The emission of Cherenkov light in air showers	11
2.2.3	The H.E.S.S. telescope system	13
2.3	The standard H.E.S.S. analysis	14
2.3.1	Data quality	14
2.3.2	Reconstruction of air showers	14
2.3.3	Gamma-Hadron separation	15
2.3.4	Background Estimation	19
3	The Method	21
3.1	The significance maps	22
3.2	Determination of the significance	23
3.3	The Monte-Carlo simulations	24
3.3.1	Basic method	24
3.3.2	Further Correlations	26
3.3.3	Differentiation within catalogues	27
3.3.4	The generalised correlation study	27
3.4	The results and error estimations	28
4	Catalogues and Results	31
4.1	Supernova remnants	31
4.1.1	Motivation	33
4.1.2	The catalogue	33
4.1.3	Distributions for the Monte-Carlo	34
4.1.4	Results	35
4.1.5	The supernova remnant G327.1-1.1	38
4.2	Star forming regions	42

CONTENTS

4.2.1	Motivation	42
4.2.2	The catalogues	42
4.2.3	Catalogue I: Distributions and Monte-Carlo	44
4.2.4	Catalogue I: Results	44
4.2.5	Catalogue II: Distributions	46
4.2.6	Catalogue II: Results	48
4.3	HII regions	48
4.3.1	Motivation	49
4.3.2	The catalogue	50
4.3.3	Distributions and Monte-Carlo	50
4.3.4	Results	50
4.4	Galactic bubbles	53
4.4.1	Motivation	53
4.4.2	The catalogue	53
4.4.3	Monte-Carlo	55
4.4.4	Results	55
4.5	OB stars and OB associations	58
4.5.1	Motivation	58
4.5.2	The catalogue	58
4.5.3	Distributions and Monte-Carlo	58
4.5.4	Results	60
4.6	Wolf-Rayet stars	60
4.6.1	Motivation	60
4.6.2	The catalogue and statistics	64
4.7	X-ray binaries	64
4.7.1	Motivation	65
4.7.2	The catalogue	66
4.7.3	Monte-Carlo	66
4.7.4	Results	66
5	Summary and outlook	69
	Acknowledgements	79

Chapter 1

Introduction

In 1912 Victor Hess discovered in a balloon experiment, that background radiation - thought to come from the ground - increased the higher he went. Hess concluded that there was radiation coming into our atmosphere from outer space and called it *Cosmic Radiation*, which later evolved to *Cosmic Rays*. In 1936, Hess was awarded the Nobel prize for this discovery.

Since the discovery of cosmic rays a lot of effort has been invested into the understanding of their origin and production. Cosmic rays are energetic particles arriving isotropically from space. About 99.8% of the cosmic rays are charged particles. The majority of the cosmic rays consist of protons and α -particles, but electrons and positrons also contribute. The energy spectrum of cosmic rays is shown in Fig. 1.1. It follows a nearly perfect power law over more than 10 orders of magnitude, however at the “knee” at 10^{15} eV and the “ankle” at 10^{18} eV the spectrum deviates from the power law. It is believed that cosmic rays below the knee are of Galactic origin, while those above originate outside the Galaxy, possibly from active galactic nuclei (AGN, see Auger Collaboration [18]).

Even after almost a century after the discovery, the knowledge about cosmic ray sources remains limited. The main complication is that the majority of cosmic rays gets deflected by interstellar and intergalactic magnetic fields, since they consist mainly out of charged particles. Only a small fraction of cosmic rays consisting out of γ -rays and neutrinos travels straight from the source to the earth (neglecting possible gravitational lensing for extragalactic sources) and therefore provides specific information about the production sites and acceleration mechanisms of cosmic rays. Experiments involving cosmic rays therefore generally focus on either γ -rays or neutrinos.

There are several experiments measuring cosmic γ -rays at different energies. The High Energy Stereoscopic System (H.E.S.S., paying homage to Victor Hess) is one of them and operates in the energy range 100 GeV - 100 TeV. It is a ground based array of Imaging Atmospheric Cherenkov Telescopes (IACT) with unprecedented sensitivity and a large field of view, allowing for the first time deep field surveys of the Galactic plane in very high energy (VHE) γ -rays. In these surveys, a large number of VHE γ -ray sources have been discovered some of which could be associated with

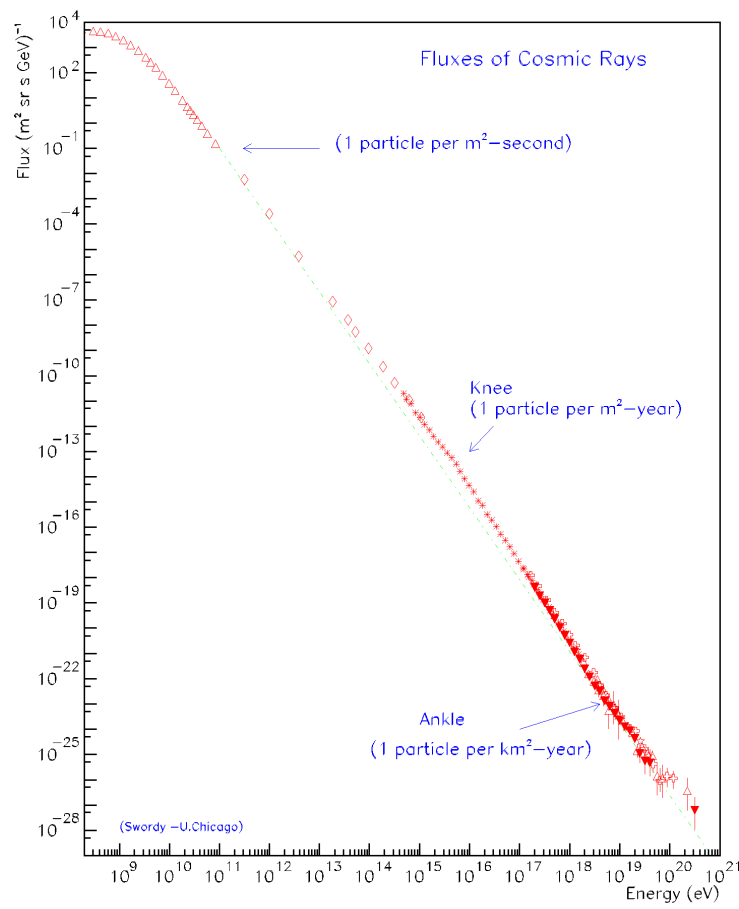


Figure 1.1: *The energy spectrum of cosmic rays (Image from [19]).*

pulsar wind nebulae (PWNe), supernova remnants (SNRs) and high mass X-ray binaries (HMXBs). However, for a considerable amount of these sources, no counterpart could be determined with certainty. In this work, an attempt is made to find statistical correlations between different types of astrophysical objects and all the Galactic H.E.S.S. sources. With this method no clear counterparts for each source are searched for, but even a general correlation or a missing correlation can give some insight on the nature or the production sites of Galactic VHE γ -rays.

In Chapter 2, production and acceleration mechanisms of VHE γ -rays, as well as the H.E.S.S. experiment and the standard H.E.S.S. analysis are described. The method used in order to find possible correlations of astrophysical objects with H.E.S.S. data is explained in chapter 3, based on a previous correlations study performed on pulsar wind nebulae by Carrigan [16]. This includes the making of the H.E.S.S. significance maps and the Monte-Carlo simulations. Finally, the various astrophysical objects, their catalogues, specific variations of the method for individual objects and the results for all objects investigated in this work are presented in chapter 4.

Chapter 2

Gamma ray astronomy with H.E.S.S.

Very high energy (VHE) γ -ray astronomy is a relatively young discipline. In the last few years, with the development of new observational techniques, VHE γ -ray astronomy has experienced a boom and the amount of known γ -ray sources has dramatically increased. The High Energy Stereoscopic System (H.E.S.S.) is an array of Cherenkov telescopes located in Namibia, and it has played an important role in the new developments.

The basic knowledge about the physics of γ -rays is described in section 2.1. In section 2.2 the H.E.S.S. experiment is presented, discussing the Imaging Atmospheric Cherenkov Telescope (IACT) method. The H.E.S.S. data analysis is described in section 2.3.

2.1 The physics of very high energy γ -rays

The term *gamma-ray* stands for photons with energies ranging from $\sim 10^5$ eV up to $\sim 10^{20}$ eV. This range of 15 decades in energy is divided into several energy bands, each being detectable by different types of telescopes. Table 2.1 gives a summary of the energy bands, as well as the kind of telescopes needed for the detection. Before the detection technique of H.E.S.S. is described in section 2.2, the production mechanisms of γ -rays are discussed in section 2.1.1 as well as the particle acceleration mechanisms in section 2.1.2.

2.1.1 Production mechanisms of γ -rays

The hottest known objects in the universe emit thermal radiation (i.e. following Planck's radiation law) up to 10 keV (X-rays), which is several orders of magnitude below the VHE range. Hence it is clear that very high energy γ -rays are of non-thermal nature. There are several mechanisms for the production of γ -rays, depending on the environments.

Band	Low/Medium	High	Very High	Ultra High
Short band	LE/ME	HE	VHE	UHE
Range	0.1-30 MeV	30 MeV-100 GeV	100 GeV-100 TeV	>100 TeV
Detection	Space	Space	Ground-based	Ground-based

Table 2.1: *The different energy ranges and detection environments of γ -rays (from [66]). The H.E.S.S. telescope system operates in the VHE-range.*

Inverse Compton scattering of electrons: When relativistic electrons interact through Inverse Compton (IC) with radiation fields, γ -rays are produced. In this process, low energy photons are up-scattered by relativistic electrons (or positrons) to γ -ray energies. Since low energy photons are found in all astrophysical objects, as well as practically everywhere else due to the cosmic microwave background, IC-scattering is a very important γ -ray production mechanism.

Decay of neutral Pions: When relativistic protons collide inelastically with matter, secondary pions and kaons are produced. The neutral pions (π^0) decay immediately (after $\sim 10^{-16}$ s) into two γ -rays. Aharonian [8] showed that above 1 GeV, for the channel $pp \rightarrow \pi^0 + X$, where $\pi^0 \rightarrow 2\gamma$, the γ -ray spectrum almost follows the power-law spectrum of the parent protons.

Bremsstrahlung: When a charged particle gets deflected by the Coulomb field of another particle, say a nucleus, then photons are emitted, since the deflection is an effective acceleration. The amplitude of the radiation is proportional to the acceleration causing the deflection.

Synchrotron radiation: Electrons moving through homogeneous magnetic fields are deflected by the Lorentz force. Only the transverse velocity is affected by the Lorentz force and the electrons are forced on a spiral movement around the magnetic field lines. Non-relativistic electrons radiate like a dipole at the Larmor frequency, while relativistic electrons also radiate a continuum spectrum.

For the production of VHE γ -rays, mainly the first two mechanisms are relevant.

2.1.2 Acceleration mechanisms of charged particles

For the production mechanisms described in the previous section, relativistic particles are required to produce VHE γ -rays. Therefore possible acceleration mechanisms are explained in this section.

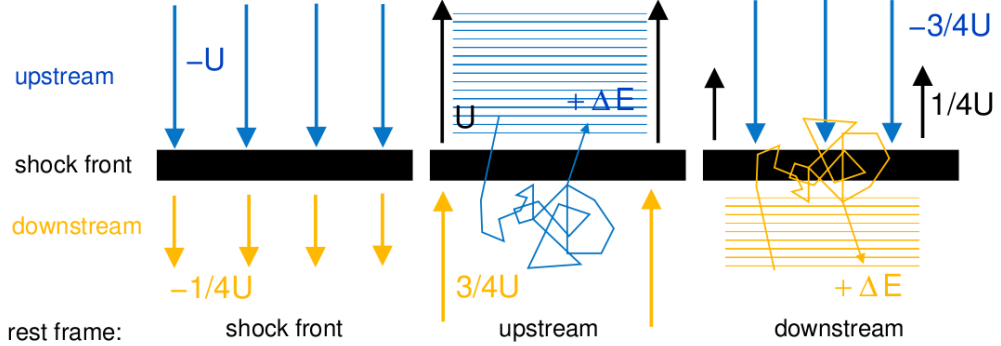


Figure 2.1: Illustration of the first order Fermi acceleration in a shock wave propagating with velocity U into an upstream medium. **Left:** Rest frame of the shock front. The upstream interstellar medium moves towards the shock front with velocity U , the downstream medium follows with velocity $1/4 U$ (if an ideal gas is assumed) with respect to the shock wave. **Middle:** Rest frame of the upstream medium. The particles at rest in the upstream medium encounter gas of the downstream region advancing with velocity $3/4 U$. Through the scattering due to the turbulences behind the shock front they become isotropic with the downstream flow and thereby gain an energy ΔE . **Right:** Rest frame of the downstream medium. The velocity distribution downstream is isotropic. Particles diffusing from behind the shock front to the upstream region encounter gas moving towards the shock front with velocity $3/4 U$. Hence the particles gain exactly the same amount of energy ΔE as in the central panel when crossing the shock front. Therefore, every time a particle crosses the shock front (in any direction) it gains energy. (Image from [39]).

First order Fermi acceleration

The first order Fermi acceleration, often called *diffusive acceleration* describes the acceleration of charged particles in shock fronts, such as in supernova remnants, termination shocks in pulsar wind nebulae or when strong stellar winds collide (see chapter 4). The idea is that relativistic particles diffuse back and forth through a shock front (e.g. from a supernova remnant) and gain energy with each passage until they leave the shocked region.

A strong shock front and a flux of particles, with velocities much higher than the shock velocity at both sides of the shock are assumed. The particles do not feel the shock, because their gyroradius is much smaller than the thickness of the shock. The turbulences behind the shock front and the irregularities in front of it ensure an isotropic velocity distribution of the particles, due to the high rate of scattering. The key point is that the distributions are isotropic with respect to the frames of reference in which the fluid is at rest on either side of the shock.

To understand how this is possible, it is useful to look at different frames of reference. When viewed in the rest frame of the region the particles originate from

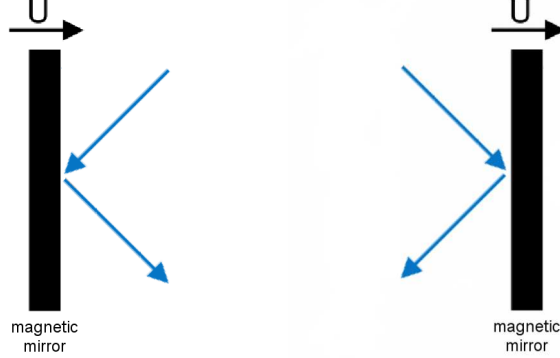


Figure 2.2: *Illustration of the second order Fermi acceleration, where particles collide with moving magnetic mirrors within interstellar clouds. **Left:** A head-on collision, where the particle gains energy. **Right:** A catch-up collision, where the particle loses energy. The key point is that the probability of head-on collisions is slightly higher than that of catch-up collisions, resulting in a net gain of energy.*

(up- or downstream), the particles diffusing into the other region get thermalised by the flow speed of the new region and gain energy (see Fig. 2.1). The charged particles bounce off magnetic inhomogeneities, generated by plasma turbulences resulting from the shock, and cross the shock multiple times. Since the process is symmetric within the rest frame of the opposite region, particles gain energy with each crossing until they escape the shock region. For a more detailed explanation, see Longair [50].

Stochastic acceleration (Second order Fermi acceleration)

The mechanism originally proposed in 1949 by Fermi was a stochastic mechanism by which particles colliding with clouds in the interstellar medium could be accelerated to high energies. Fermi proposed that charged particles are reflected from *magnetic mirrors* associated with irregularities in the Galactic magnetic field. There are two possible types of collisions with these randomly moving mirrors: head-on collisions and catch-up collisions (see Fig. 2.2), where there is a net gain and loss of particle energy respectively. Fermi showed that the particles gain energy statistically in these reflections, since there is a slightly greater probability of head-on collisions in comparison to the catch-up collisions.

In his original paper [38], Fermi assumed that this mechanism would be the main source of energy for the particles. However, several problems are encountered. The rate of such collisions in interstellar clouds is too small to account for a significant gain in energy, but small-scale turbulences might help. Furthermore, the energy losses have to be considered, since in particular ionisation losses make the energy gain of low energy particles difficult. To overcome the energy loss, particles

with high enough energies must either be injected into the acceleration region or the acceleration process must be fast enough.

Since Fermi's publication several attempts have been made to solve these and other problems. One adaptation of the mechanism is the first order acceleration described in the previous section. However there are also modern versions of second order Fermi acceleration, where the particles interact with various types of plasma waves and gain energy by being scattered stochastically by these waves. More details can be found in Longair [50] and references therein.

2.2 The H.E.S.S. experiment

The H.E.S.S. experiment (High Energy Stereoscopic System) is a system of Imaging Atmospheric Cherenkov Telescopes (IACTs). The name should remind of Victor Hess who obtained the Nobel Prize in 1936 for discovering cosmic rays in balloon experiments. H.E.S.S. is an array of four IACTs located in the Khomas Highlands in Namibia. The site provides excellent conditions for astronomical observations and offers the possibility to observe the inner regions of the Galactic plane with high altitude above the horizon. Cherenkov telescopes use the Earth's atmosphere as detector material, since VHE γ -rays cannot be detected directly (the fluxes in the energy range are too low for satellite telescopes). What is in fact detected is the Cherenkov light emitted by air showers, i.e. cascades of secondary particles which are produced in the interaction of γ -rays with the atmosphere. In the following, the air showers required for H.E.S.S. to detect γ -rays, the Cherenkov light they emit, as well as the H.E.S.S. telescope array itself are described in sections 2.2.1 through 2.2.3.

2.2.1 Air showers

When cosmic rays enter the atmosphere, they interact with atmospheric particles, such as atomic nuclei, producing secondary particles. If the initial energy is in the TeV range, the secondary particles also interact with atmospheric particles, producing some more particles, which can in turn also interact, and so forth. This way, an air shower develops. There are two types of air showers - electromagnetic and hadronic - depending on the nature of the primary particle.

Electromagnetic showers

Electromagnetic showers occur whenever VHE particles which interact via electromagnetic interactions traverse matter. There are two possible interaction processes: bremsstrahlung and pair production. Bremsstrahlung was described in section 2.1.1. If the energy of a photon is at least twice as high as the rest mass of electrons, then the photon can produce an electron-positron pair. However because of momentum and energy conservation, this process can only occur in the field of another particle, e.g. a nucleus, which takes the recoil as the third reaction partner.

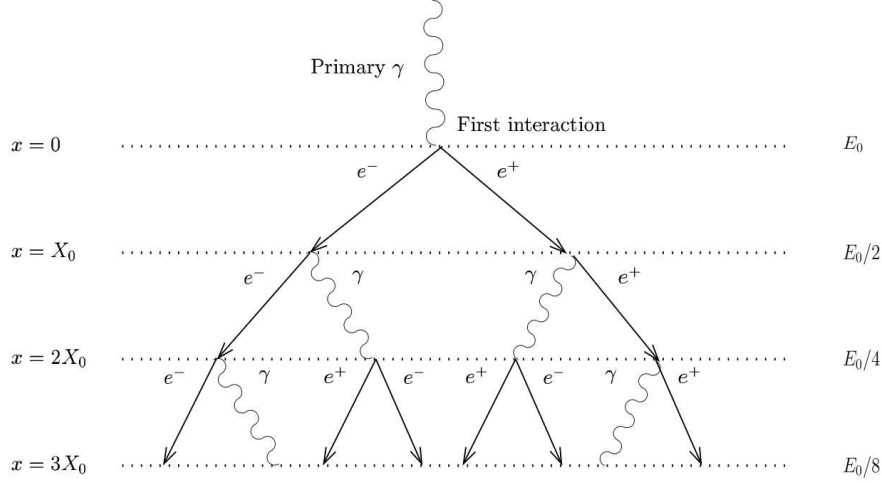


Figure 2.3: A simple model for the electromagnetic shower according to Bethe and Heitler [44]. Only bremsstrahlung and pair production are considered and the mean free paths X_0 are assumed to be equal for both processes. Furthermore, it is assumed that the energy is divided equally between the particles. The atmospheric depth is denoted as x and the energy per particle by $E_0/2^x$. (Image from [39])

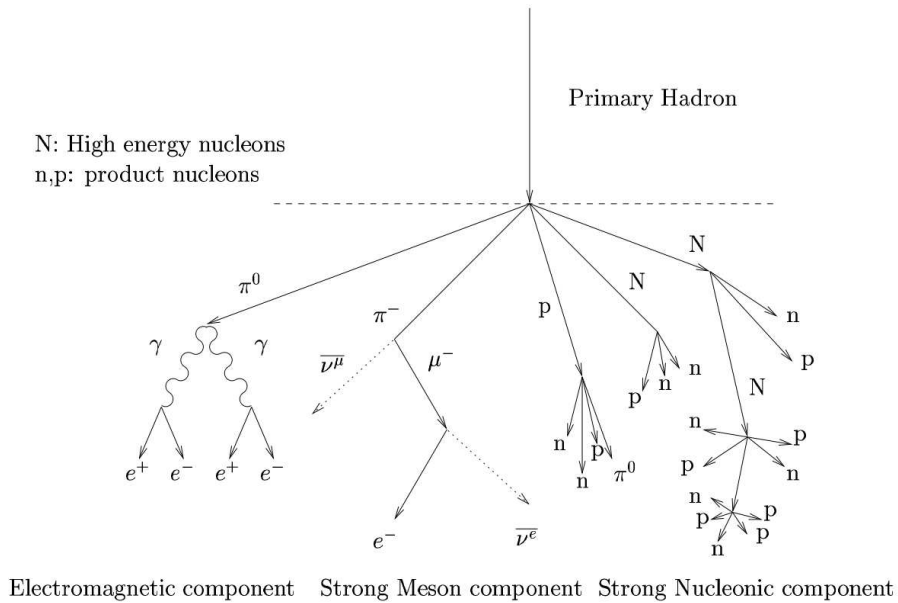


Figure 2.4: A simple model for the hadronic shower with different components. The lengths of the arrows are not to scale with the lifetime of the particles. (Image from [39])

In an electromagnetic shower, these processes happen successively. The length of the shower depends on the characteristic length scale for these interactions, which is the mean free path length X_0 . This is the radiation length for bremsstrahlung and the conversion length for pair production. The Coulomb scattering of the secondary particles off the atmospheric nuclei determines the width of the shower. A simple model of the shower development is shown in Fig. 2.3. The number of particles increases exponentially until reaching the shower maximum. The maximum number of particles is proportional to the energy of the primary particle. When the mean particle energy drops below ~ 80 MeV, the production of new particles stops, since the electrons mainly lose their energy through ionisation.

Hadronic showers

Hadronic showers are more complex than electromagnetic showers. This is not only because strong interactions themselves are more complex, but also because electromagnetic subshowers can develop as well. When a hadron interacts with particles in the atmosphere, strong interactions dominate and different particles like mesons (π , K), nucleons (p , n) and hyperons (Λ , Σ , Ξ) are created. These secondary particles are at the origin of hadronic showers. The electromagnetic subshowers mainly develop after the decay of neutral pions into two photons. Charged pions decay mainly into muons which in turn decay into electrons and neutrinos. However the charged pion's longer lifetime increases the chance of interacting with other atmospheric particles, resulting in hadronic subshowers. The produced muons do not interact much and often escape from the shower. Figure 2.4 shows a schematic view of a hadronic shower. The particles involved in weak and strong interactions receive higher transverse momenta by inelastic scattering than electromagnetic particles, resulting in a much broader lateral extension of hadronic showers as compared to electromagnetic showers (Fig. 2.5).

2.2.2 The emission of Cherenkov light in air showers

When charged particles move through matter with velocities higher than the phase velocity of light in the medium, they emit Cherenkov radiation. This radiation is comparable to the sound emitted when planes fly at supersonic velocities. The charged particles locally polarise the medium as they traverse it. When the medium regains equilibrium, photons are emitted which in normal circumstances interfere destructively with each other. However, when a particle travels faster than light in that medium, the photons constructively interfere and intensify the observed radiation.

When VHE cosmic rays enter the atmosphere, they transfer enough energy to the secondary particles to emit Cherenkov radiation. This bluish light is emitted in a cone around the trajectories of the particles. Usually the Cherenkov radiation of electromagnetic showers reaches the ground in a circle with a radius of 80 - 150 m. Comparisons of simulated electromagnetic and hadronic showers and light distributions on the ground are shown in Figs. 2.5 and 2.6.

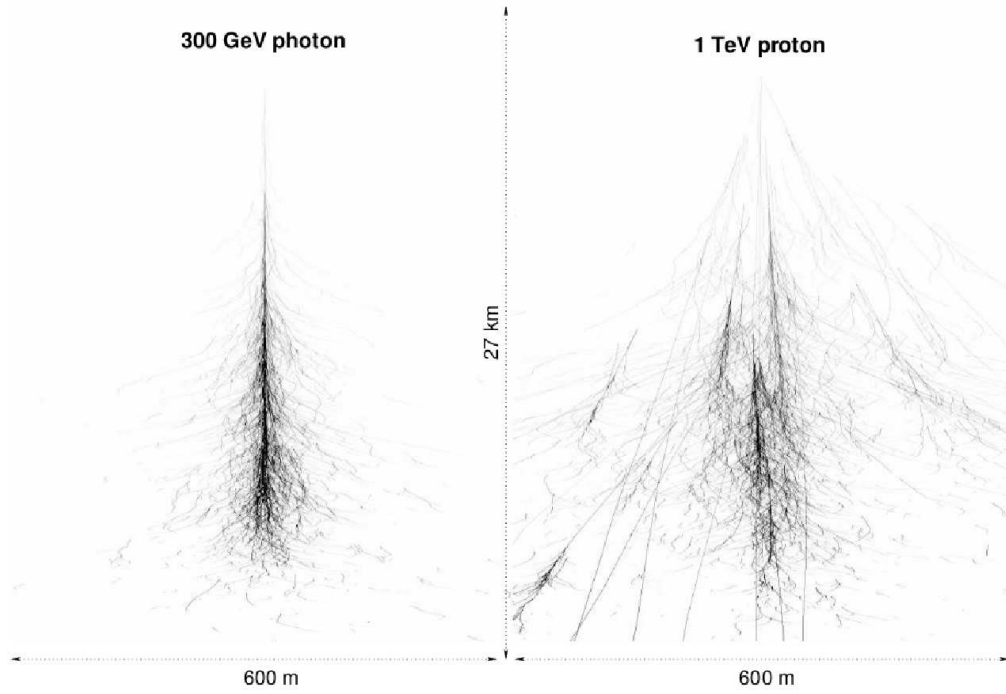


Figure 2.5: *Simulated particle trajectories for a 300 GeV photon and a 1 TeV proton (Image from [13]).*

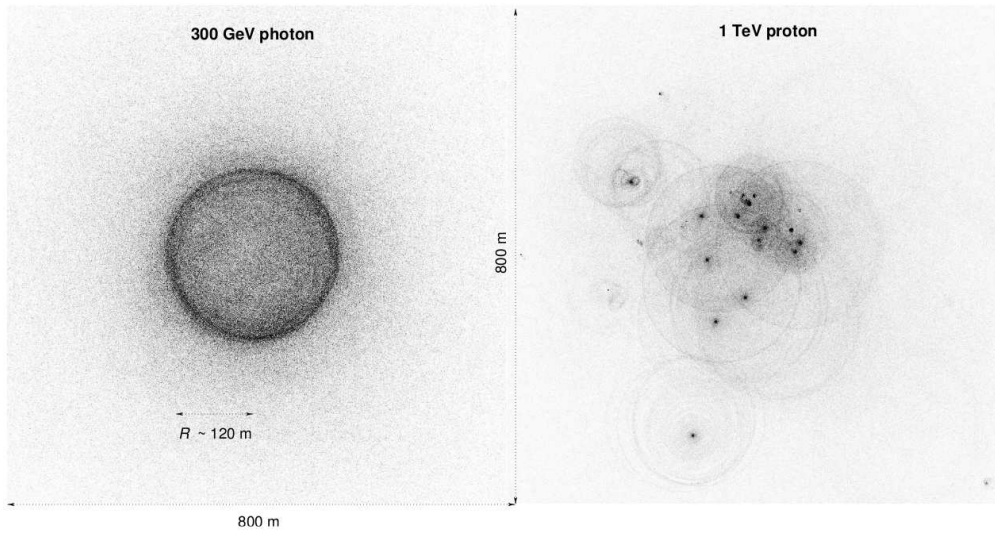


Figure 2.6: *Simulated Cherenkov light distribution for a 300 GeV photon and a 1 TeV proton (Image from [13]).*

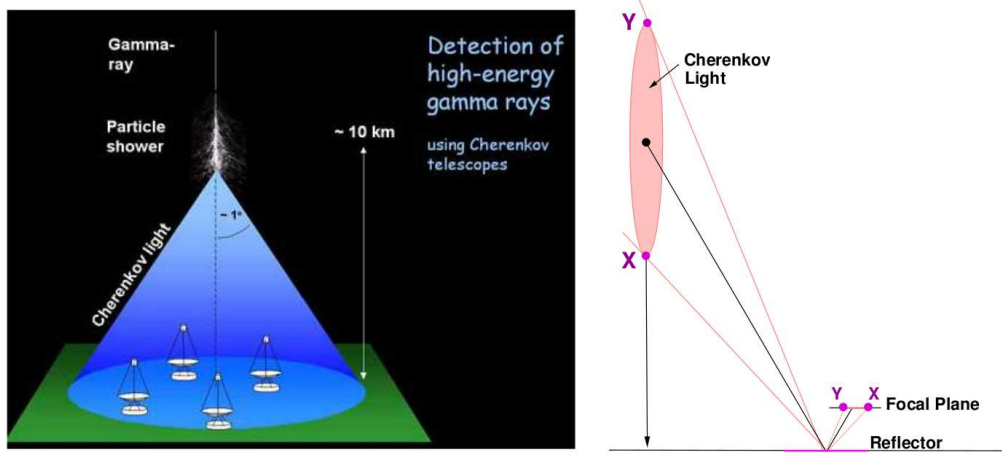


Figure 2.7: **Left:** *The Imaging Atmospheric Cherenkov Technique (by W. Hofmann).* **Right:** *Reflection of the shower image onto the camera. (Image from [16]).*

2.2.3 The H.E.S.S. telescope system

As mentioned before, H.E.S.S. is an array of IACTs located in Namibia. Four 13 m diameter Cherenkov telescopes are positioned at the corners of a 120 m square, in order to provide multiple stereoscopic views of air showers (important for the direction reconstruction) and to achieve a better sensitivity. Each telescope has 382 circular mirrors with a diameter of 60 cm each arranged in a Davies-Cotton design [20], which gives a mirror area of $\sim 108 \text{ m}^2$ per telescope. This permits a low energy threshold of 100 GeV in the best case of small zenith angles. The Cherenkov light is reflected onto a camera located in the focal length (15 m), which has a 5° field of view and consists out of 960 photo-multiplier tubes (PMTs). The large field of view allows observations of extended sources and surveys (see section 3.1), while the small pixel size (0.16°) enables to resolve details. A central trigger selects the events which are detected by at least two of the four telescopes, reducing thereby the dead time. To improve the sensitivity even further, the H.E.S.S. array is currently being upgraded to H.E.S.S. Phase II. A fifth telescope with a mirror area of 600 m^2 will be located at the centre of the current H.E.S.S. array.

Figure 2.7 shows the detection principle of H.E.S.S. schematically. VHE cosmic rays interact with atmospheric nuclei and generate air showers whose secondary particles emit Cherenkov light. Telescopes located within the light cone can detect the air shower. The right panel of Fig. 2.7 shows schematically how the image of a shower is reflected onto the camera in the focal plane. The angle under which the shower is observed determines the length of the image, while the distance of the shower to the ground determines the position on the camera. The width of the image gives information about the lateral extend of the shower, enabling the distinction between electromagnetic and hadronic showers (see section 2.3.3), since

the hadronic showers are generally broader than electromagnetic showers.

2.3 The standard H.E.S.S. analysis

There are several steps in the analysis of the data obtained by the telescope array. First the quality and possible systematics of the data have to be checked (section 2.3.1). Then the direction and the energy of the primary particles can be reconstructed from the H.E.S.S. standard analysis (section 2.3.2). Furthermore, it is necessary to separate signals coming from γ -rays and those coming from hadrons (section 2.3.3), in order to reduce the background (section 2.3.4).

2.3.1 Data quality

There are several effects reducing the data quality, from which especially the energy reconstruction suffers.

Atmospheric effects: The atmosphere is constantly changing in density, temperature, pressure and humidity. This affects the detector response. Furthermore the Cherenkov light can be absorbed due to dust and clouds. It is therefore necessary to take observations under good and stable conditions to avoid systematic effects on the measured flux.

Camera response: The camera response is given by the single photo-electron response and the quantum efficiency of each PMT. A LED system mounted in front of the camera monitors the single photo-electron gain of the PMTs. Differences between the PMTs are flat-fielded using a laser mounted on the telescope dish. See Aharonian [26] for a detailed description of the calibration.

Optical response: The decrease in reflectivity of the mirrors with time is one of the factors affecting the optical response of the instrument. This response is monitored in dedicated muon-runs, in which no coincidence between telescopes is needed and where the Cherenkov light from single muons passing close to the telescope are studied. See Bolz [15] for a detailed description.

2.3.2 Reconstruction of air showers

Since VHE particles are not detected directly, their properties like type, energy and direction have to be reconstructed from the observed images of the air showers they produce. Compared to single IACTs like Whipple [5] and MAGIC [4] (before the extension to MAGIC II), H.E.S.S. has the great advantage of being an *array* of IACTs, recording the air showers from different viewing angles. This improves the reconstruction of the primary particle's properties significantly. The following steps are applied:

Image cleaning: In order to remove noisy pixels containing mainly night sky background and to keep the pixels with Cherenkov light, a two level filter is used

(after calibration of the light intensity distribution in the camera). Only pixels which show a signal of at least 10 photo-electrons (p.e.) and have a neighbouring pixel with at least 5 p.e. - or vice versa - are kept (see Fig. 2.8). In this way, spatially correlated features which can be used for the next steps of the analysis are obtained.

Hillas parameters: The Hillas parameters (see Hillas [46]) describe the features of the elliptical images obtained after the image cleaning. Figure 2.9 shows schematics of the Hillas parameters. They give information about the shape of the ellipse (width and length), the light intensity (image amplitude) and the position and orientation of the ellipse in the camera.

Direction reconstruction: The direction from which the primary particle originated can be found using at least two stereoscopic images of the same air shower. The intersection of the major axes of all images gives the reconstructed direction (see Fig. 2.10). Only images which are well inside the camera and which are of sufficient intensity are used. H.E.S.S. achieves an accuracy in direction reconstruction (point spread function) of $\sim 0.1^\circ$.

Energy reconstruction: To reconstruct the energy of the primary particle, the measured signal of the shower is compared to Monte-Carlo simulations. The energy from the observed γ -rays is determined using the mean of the energies independently estimated for each telescope. The parametrisation of energies from Monte-Carlo simulations depend on the image amplitude, the reconstructed impact parameter (i.e. the distance of the impact point of the shower on the ground and the telescope) and the zenith angle of observation for the telescope system. The energy reconstruction is particularly sensitive to the systematic effects described in section 2.3.1.

2.3.3 Gamma-Hadron separation

The vast majority of reconstructed air showers come from hadronic cosmic rays and form the cosmic ray background. To separate γ -like from non- γ events, cuts on image parameters have to be applied.

Shape cuts: These cuts make use of the difference in the shape of the light intensity distribution of γ -rays and hadrons. The mean reduced scaled width (MRSW) and mean reduced scaled length (MRSL) of the image are compared to simulations. The scaled width is $w_{sc} = (w - \langle w \rangle) / \sigma_w$, with w the width derived from the image, $\langle w \rangle$ the expected value from simulations of the mean width and σ_w the standard deviation. By averaging over all participating telescopes the MRSW is obtained. The same method is applied to derive the MRSL. Figure 2.11 shows a comparison of the MRSW and MRSL between the data and the simulated γ -rays and hadrons.

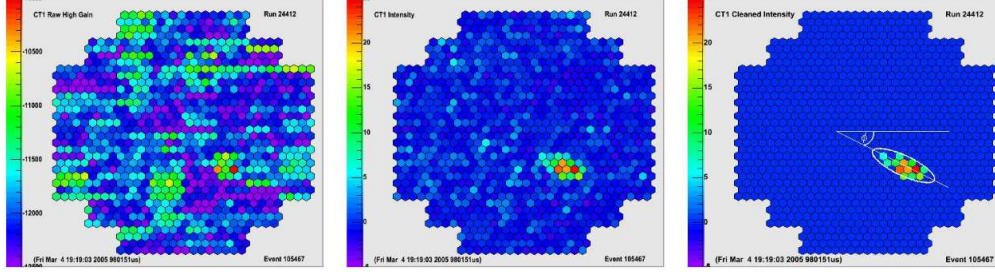


Figure 2.8: An air shower image in different stages of the analysis. **Left:** Raw photo-electron counts after baseline subtraction. **Middle:** Calibrated image with pixel intensities in photo-electrons. **Right:** The same event after cleaning. The image parametrisation is shown (see Fig. 2.9). (Images from [40]).

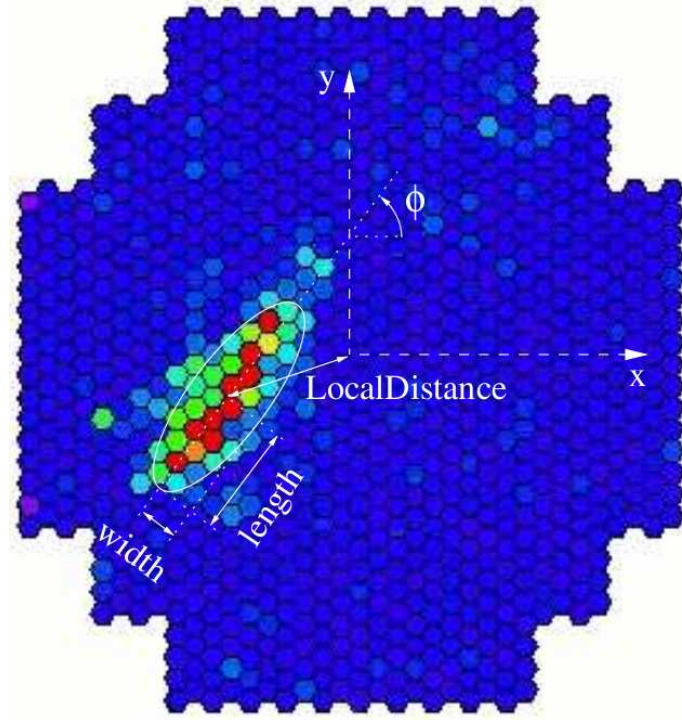


Figure 2.9: Hillas parameters for a γ -ray event, which can be approximated as an ellipse. (Image from [24]).

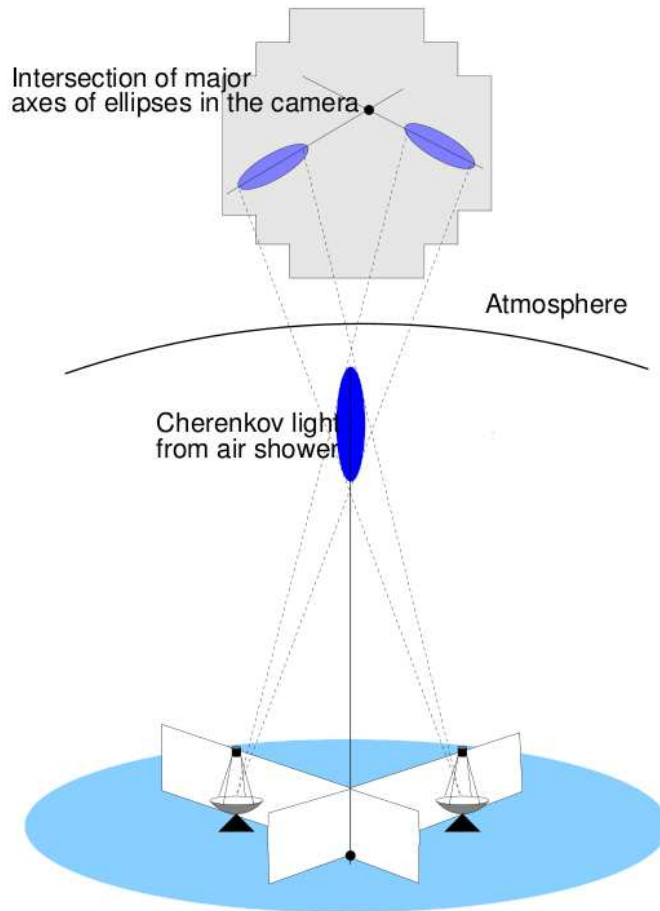


Figure 2.10: *Schematic description of the direction reconstruction. The intersection of the major axes of all images gives the reconstructed direction. (Image from [39]).*

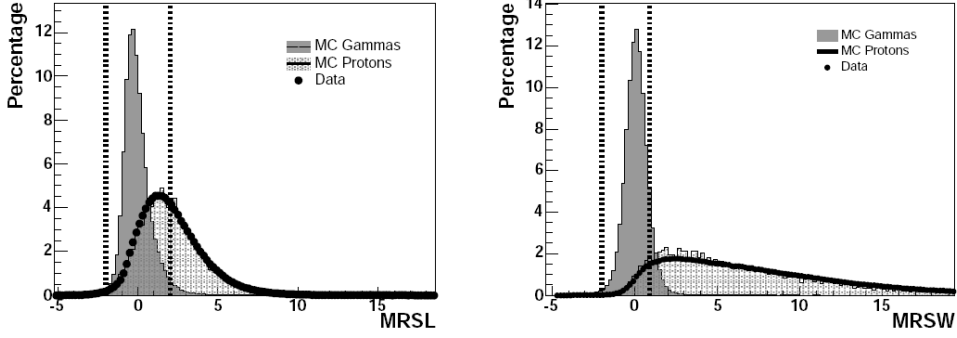


Figure 2.11: *Distribution of MRSL (left) and MRSW (right) for Monte-Carlo simulated γ -rays and protons and for off-source data without application of any image cuts. (Image from [39]).*

θ^2 -cuts: A directional cut on the squared angular difference between the reconstructed shower position and the source position (θ^2) is applied. Since the γ -rays come directly from the source, while the charged cosmic rays are deflected by interstellar and intergalactic magnetic fields and therefore arrive isotropically, this cut further suppresses the residual hadronic background.

Different cuts can be applied - standard and hard cuts - depending on the nature of the observed source. The standard cuts use a size cut of 80 p.e. and an optimal θ^2 cut of 0.02° , whereas the hard cuts use a size cut of 200 p.e. and a θ^2 cut of 0.01° . The hard cuts have the advantage of reducing the background by a factor of 7 and yield optimum sensitivity for weak sources (e.g. extragalactic sources), provided that the source energy spectra are not too steep. The standard cuts have the advantage of a lower energy threshold in comparison to the hard cuts which is especially desirable in the determination of energy spectra of Galactic sources. The cuts are summarised in Table 2.2.

Configuration	MRSL	MRSW	θ^2	Image Amp.	Distance
	Min / Max	Min / Max	Max (deg. ²)	Min (p.e.)	Max (deg.)
Standard	-2.0 / 2.0	-2.0 / 0.9	0.02	80	2.0
Hard	-2.0 / 2.0	-2.0 / 0.9	0.01	200	2.0

Table 2.2: *Summary of cut parameters*

2.3.4 Background Estimation

To extract signals from positions on the sky, it is essential to remove the background. Different approaches are possible, but all have in common, that the significance of the excess will be calculated using the likelihood ratio method described by Li and Ma [47], where the *on*-events are calculated in a circle with radius θ . The differences lie in the various ways of defining the *off*-regions, where the background is determined.

Ring background: The background in this method is calculated from a ring around the observed position (Fig. 2.12). The width of the ring is set such that its area is ~ 7 times larger than the area of the *on*-region. To account for the change of the radial background acceptance in the camera, a weight factor is added to the normalisation of the areas. Because of the possible change of acceptance with energy and the resulting uncertainty in background levels over the whole energy range, this method is not used to derive spectra. However, this method is used to make the significance maps of the Galactic plane.

Reflected background: In this method, seven *off*-regions are used, which have the same size as the *on*-region. *On*- and *off*-regions lie on a circle centred on the observation position, with equal distances between them. These regions are shown in Fig. 2.12 as circles filled with diagonal lines. This method has the advantage that all regions have the same radial background acceptance. It is ideal for flux measurements and for deriving spectra.

These are the background estimation methods used in this work. These and other background estimation methods are described and discussed in more details in Berge et al. [12].

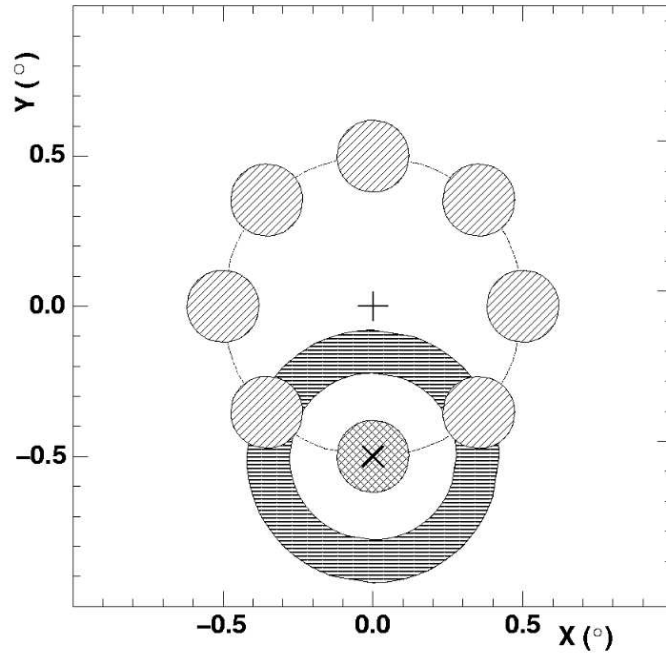


Figure 2.12: The background regions for two different methods: the reflected background regions filled by diagonal lines, the ring background region filled by horizontal lines. The on-region is filled with cross hatched lines. The cross marks the observation position. (Image from [28])

Chapter 3

The Method

This chapter describes the method used for the correlation study of astrophysical objects with H.E.S.S. data. The method is based on a correlation study of pulsar wind nebulae (PWNe) with H.E.S.S. data by S. Carrigan [16], in which all pulsars from the Parkes Multi-beam Pulsar Survey (PMPS) [35] with positions within the range of the H.E.S.S. Galactic scan are checked for a significant VHE γ -ray excess. The goal of this study is to estimate the rate of chance coincidences using Monte-Carlo simulations.

In the correlation study by Carrigan [16] a H.E.S.S. sky map is used to determine the significance of a VHE γ -ray signal at the pulsar's positions. The PMPS pulsar catalogue [35] is then modelled with Monte-Carlo simulations, in order to create random samples of “pulsars”, which follow the distribution of the PMPS pulsars. The significance of the VHE γ -ray excess at the Monte-Carlo pulsar's positions is determined from the same map as for the data, in order to estimate the chance coincidences between PMPS pulsars and VHE γ -ray sources.

In this work, the method has been generalised to be applied to other catalogues of astrophysical objects, including the possibility to investigate objects of different sizes (e.g. HII regions) or objects that can be divided into several subclasses (e.g. supernova remnants). Furthermore, the analysis has been adapted to investigate the dependences on different physical quantities, some of which might be correlated, such as the surface brightness of extended objects which depends on the size and the flux density. All this has to be considered in the Monte-Carlo simulations making significant additions and adaptations to the existing method necessary.

In section 3.1 it is described how the H.E.S.S. significance maps are made, while the different possibilities to determine the significance of the VHE γ -ray signal are discussed in section 3.2. The Monte-Carlo simulations are explained in section 3.3. Finally the results and error estimations are discussed in section 3.4.

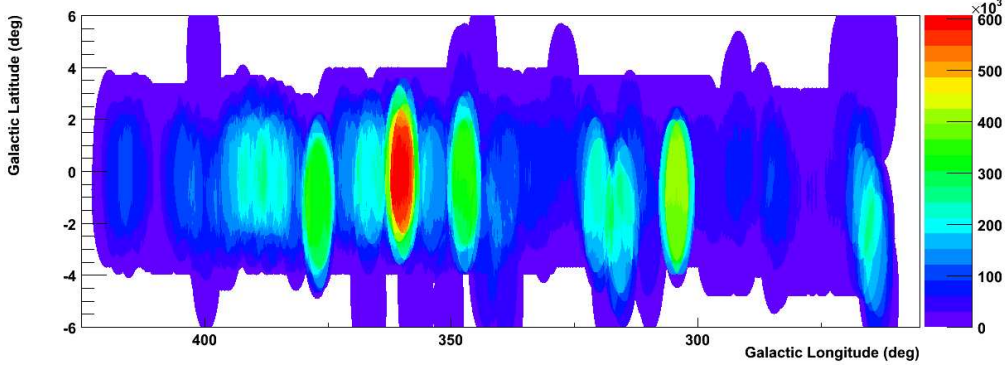


Figure 3.1: The H.E.S.S. exposure time in seconds in the region $-105^\circ < l < 65^\circ$, $|b| < 5^\circ$. It can be seen that the exposure is not uniform over the whole area. For example the Galactic centre has a clearly higher exposure time than the rest of the Galactic plane.

3.1 The significance maps

For each catalogue, the significance of the VHE γ -ray excess of each object is determined from a H.E.S.S. significance map. To make the significance maps for the correlation study, all the H.E.S.S. data available until August 2008 in the Galactic range $-105^\circ < l < 65^\circ$, $|b| < 5^\circ$ were used. This includes the published data from the H.E.S.S. Galactic plane survey [27], [29], as well as an extension from $-105^\circ < l < -30^\circ$, dedicated observations and re-observations of Galactic sources. In total, 3311 runs of usually 28 minutes each with a total corrected live time of ~ 1515 hours were used. Figure 3.1 shows a map of the exposure time for this data set.

To compute the significance at each position in the map the following parameters are needed:

- N_{on} : The number of events in the circular *on*-region with radius θ , centred on the position.
- N_{off} : The number of events in a ring region (see section 2.3.4) around the position, with an area seven times the *on*-region.
- α : The normalisation factor, which accounts for the difference in solid angle for N_{on} and N_{off} and for the variation of the acceptance for γ -ray showers within the field of view, as well as with zenith angle and exposure time.

With these parameters, the significance of the signal above background can be determined using the standard approach described by Li and Ma [47].

In this work, the correlation radius θ needed for the determination of N_{on} is chosen for each catalogue individually. If the catalogue does not provide information

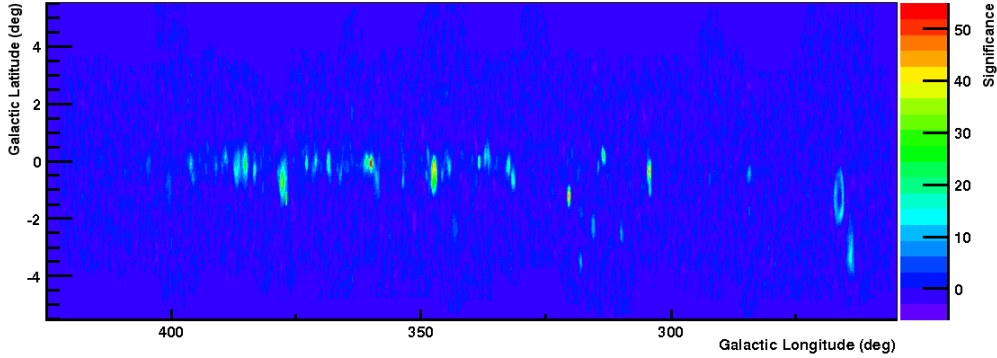


Figure 3.2: A *H.E.S.S.* significance map in the region $-105^\circ < l < 65^\circ$, $|b| < 5^\circ$, with $\theta = 0.22^\circ$.

on the size of the objects, a correlation radius of either $\theta = 0.1^\circ$ or 0.22° for point-like or slightly extended sources respectively will usually be used. For catalogues with information on the size of the objects, three approaches can be used to determine the significance, as will be seen in section 3.2: either a map of the whole Galactic plane with $\theta = 0.1^\circ$ is used and the maximum significance will be looked up within the object's extend, or a set of maps with different θ values are created and the significance is looked up from the map with the corresponding θ , or a smaller map for each object with a correlation radius θ comparable to the objects size will be created. These smaller maps are created in the same way as are the maps of the Galactic plane, only for a smaller region and generally greater radius θ . In Fig. 3.2 a significance map of the H.E.S.S. scan region is shown.

3.2 Determination of the significance

For the correlation study of PWNe with H.E.S.S. data [16], the significance of the H.E.S.S. signal was determined at the position of the pulsars from the Parkes Multi-beam Pulsar Survey (PMPS) [35] in a significance map with a correlation radius of $\theta = 0.22^\circ$ for slightly extended objects, to account for the nebulae that are not point sources like the pulsars themselves. This way of extracting the significance can be used for all objects of similar type or if no size information is given. If the objects are clearly extended, it is preferable to take into account the any given size information.

Since most of the extended sources have a variety of sizes, there are two basic possibilities to get a significance. One way is to get the significance at the object's position in a map with a correlation radius of the same order as the radius of the object. This can either be done by creating for each single object a significance map of the surroundings with the object's size as correlation radius or by making several maps of the Galactic plane scan region with different correlation radii and choose the

right map depending on the object's size. Larger ring radii in the Ring Background method (section 2.3.4) demand better accuracy for the relative acceptance correction across a larger portion of the field of view, setting a limit to the maximal correlation radius used to $\theta_{\max} = 0.4^\circ$. The second method is not as exact as a specific map for each object, but it is much less time consuming. If the number of objects in the catalogues is large the second method is used, otherwise the first method is preferable.

The other way to get the significance is to take a significance map with a correlation radius for point sources (i.e. $\theta = 0.1^\circ$) and search for the maximal significance within the object's radius. This method would especially be useful for objects like shell type supernova remnants, where the VHE γ -ray emission is expected mainly in the outer regions of the remnant. This method is also much less time consuming as the map-making method. All three methods - the set of maps, the maximum-searching and the map-making method (in order of increasing time consumption) - are implemented in the generalised MC.

Since there are some VHE γ -ray sources whose counterpart is determined with absolute certainty (e.g. HESS J1713-397 / RX J1713.7-3946), these sources are excluded when determining the significance of the VHE γ -ray signal of the objects. Only if the counterpart is of the same nature as the objects in question, as in the case of the SNR RX J1713.7-3946 in the SNR correlation study, the known source is included.

3.3 The Monte-Carlo simulations

To estimate the rate of chance coincidences of objects from astrophysical catalogues with VHE γ -ray signals, these catalogues are simulated via Monte-Carlo simulations. For the Monte-Carlo it is necessary to consider any trend relevant physical quantities might have. Furthermore, trends that reflect a purely observational feature have also to be included in the MC, since the observed and possibly incomplete catalogues will be compared to the simulated catalogues. This comparison only makes sense, if the incompleteness is also modelled. The catalogue used for the PWN correlation study [16], i.e. the Parkes Multibeam Pulsar Survey (PMPS) [35], can be modelled quite easily and will be used as an example to illustrate the basic method.

3.3.1 Basic method

For the Monte-Carlo only pulsars within the search region ($-105^\circ < l < 65^\circ$, $|b| < 5^\circ$, exposure > 2 hours) are considered. The pulsar catalogue contains 1789 pulsars, of which only 649 are within the H.E.S.S. Galactic plane survey area.¹ A statistically meaningful amount of random samples (10^5 - 10^7) containing each n pulsars is created where n is picked from a Gaussian distribution with mean 649 and width

¹In [16] only 435 pulsars are located in the H.E.S.S. Galactic plane survey area, since at that time less data was available. Therefore the distributions and results of the pulsar correlation study shown here differ slightly from those in [16].

$\sqrt{649}$. The results of the Monte-Carlo are then scaled by the number of simulated samples to enable the comparison to the original catalogue.

In the left panel of Fig. 3.3 it can be seen that pulsars with higher spin-down energy fluxes at Earth $\dot{E}/(4\pi d^2)$ (where \dot{E} is the spin-down energy and d is the distance to the pulsar) seem to be located closer to the Galactic plane. This is expected, since it is assumed that pulsars are born with a kick velocity which often moves them away from their birth place in the Galactic plane and because they lose some of their spin-down energy flux while they get older. This important characteristic feature of the PMPS catalogue has to be taken into account for the Monte-Carlo simulation.

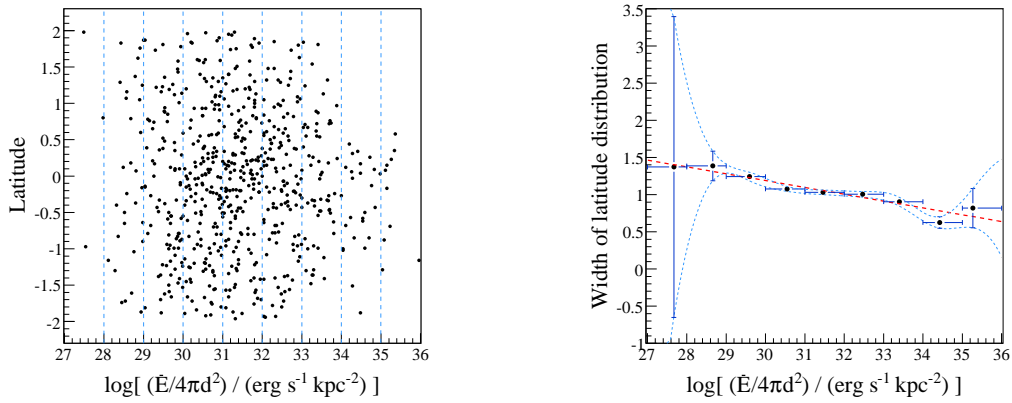


Figure 3.3: **Left:** The spin-down energy flux distribution of the PMPS pulsars [35] within the H.E.S.S. Galactic plane survey region as a function of the Galactic latitude. The pulsars with higher spin-down energy flux seem to be located closer to the Galactic plane. In each of the bands delimited by the blue dashed lines, a Gaussian is fitted to the latitude distribution. **Right:** The widths of the Gaussians (fitted to the latitude distribution) as a function of $\log[\dot{E}/4\pi d^2]$. The vertical error bars are the errors on the widths from the respective Gaussian fits, while the horizontal error bars show the width of each $\log[\dot{E}/4\pi d^2]$ -band. The red dashed straight line is a fit to the widths, while the thin blue dashed lines follow the error bars.

The simulation is done as follows: the catalogue data are divided into bands of $\log[\dot{E}/4\pi d^2]$ and a Gaussian is fit to the distribution of pulsars in each of these bands denoted by blue dashed lines in the left panel of Fig. 3.3. The widths of these Gaussians are plotted as a function of $\log[\dot{E}/4\pi d^2]$ (right panel). For each MC-pulsar, a random value for $\log[\dot{E}/4\pi d^2]$ is picked from the fit to the spin-down energy flux distribution of the pulsars (Fig. 3.4) and the corresponding Galactic latitude is then determined from a Gaussian with a width taken from the fit in the right panel of Fig. 3.3. If the width of the latitude distribution is negative (e.g. in the lower blue dashed line), then 0.01 is taken as a value for the width. The Galactic longitude is taken randomly from the fit to the pulsar's longitude distribution shown

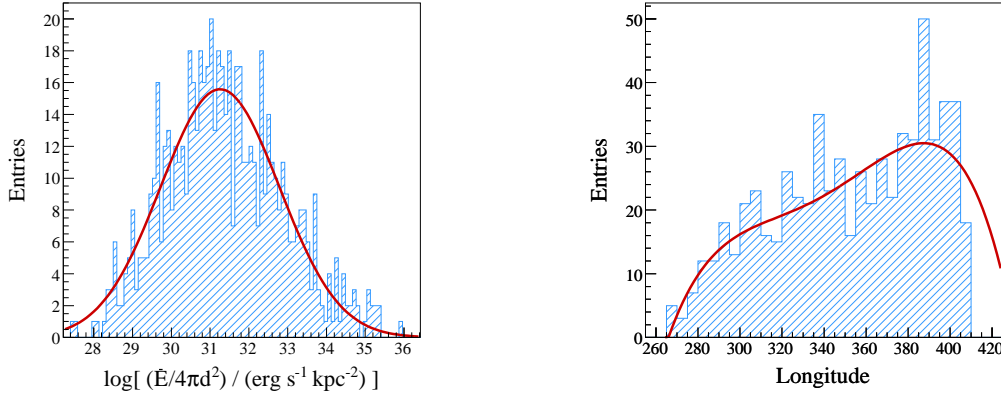


Figure 3.4: **Left:** The spin-down energy flux distribution of the PMPS pulsars [35] within the H.E.S.S. Galactic plane survey region. **Right:** The longitude distribution of the pulsars within the H.E.S.S. Galactic plane survey region.

in the right panel of Fig. 3.4, since no particular correlation is found.

3.3.2 Further Correlations

While the process described above is sufficient for the PWNe, it will be shown in chapter 4 that other catalogues need a more complex modelling. If two or more physical quantities of a class of astrophysical objects are correlated the matter is slightly more complicated. This will be illustrated using the surface brightness for extended objects, such as supernova remnants.

The surface brightness at a frequency ν is related to the size and the flux density via the relation

$$S_\nu = \frac{F_\nu}{4\pi\theta^2} \quad (3.1)$$

where F_ν is the flux density at the frequency ν and θ is the angular radius in radians. Usually the radius and the flux density are not only correlated with each other but also with the Galactic latitude and sometimes the longitude. For supernova remnants, the correlation of the latitude with the radius is modelled in the same way as the correlation with the spin-down energy flux for pulsars in section 3.3.1. The correlation of the radius and the flux density is then modelled in a similar way. A first order polynomial is fit to the distribution of the correlated quantities (Fig. 3.5, left), while its mean width is determined from Gaussians fitted to the data in the bands denoted by the blue dashed lines. Since the width is generally assumed to be roughly the same over the whole distribution, a constant is fitted to the values of the width (Fig. 3.5, right). Unfortunately, the bands are not perpendicular to the fit function, which results in an uncertainty in the width. A different approach has been tested where the bin sizes were adapted so that each bands contains the same number of entries, but no significant changes were observed.

A random value for the radius is picked from the radius distribution of the supernova remnants in the catalogue and the corresponding flux density is determined from a Gaussian with the corresponding mean and width from the fits in the left and right panel of Fig. 3.5 respectively. The main difference to the latitude correlation is therefore, that the mean value in each band has to be determined and that the width is assumed to be constant, while the opposite applies for the latitude.

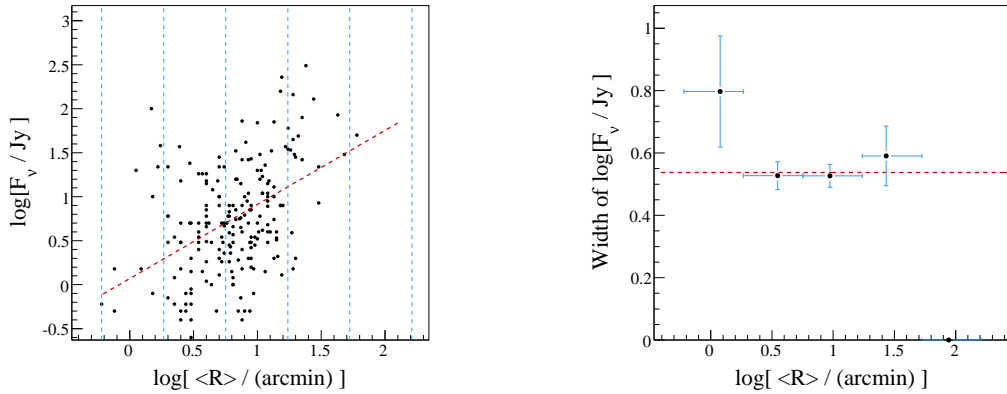


Figure 3.5: Left: The distribution of the flux density of supernova remnants from Green’s catalogue [43] as a function of their mean radius. The red dashed line is the fit through the distribution. **Right:** The width of the flux density vs. radius distribution of SNRs, determined from Gaussian fits in the bands denoted by the blue dashed lines in the left panel. The vertical error bars are the errors on the widths from the respective Gaussian fits, while the horizontal error bars show the width of each $\log[\langle R \rangle]$ -band.

3.3.3 Differentiation within catalogues

Some astrophysical objects come in different types or subclasses, e.g. the supernova remnants which can be shell type, composite or filled centre supernova remnants. To make correlation studies for the different subclasses, these subdivisions have to be taken into account by the simulations. Unfortunately this differentiation varies for different astrophysical objects, which makes a generalisation difficult. Therefore, the specifics of this problem are described separately for the different objects in chapter 4.

3.3.4 The generalised correlation study

The general method applicable to most of the catalogues has been described in the previous sections. In some cases some minor adjustments have to be made, which will be described individually for each catalogue in chapter 4. The differences

Pulsar-only MC	Generalised MC
same correlation radius for all pulsars	different correlation or search radii accounting for different sizes
one type of objects	differentiation between subtypes within one catalogue possible
one physical quantity ($\dot{E}/4\pi d^2$) correlated with latitude	several physical quantities correlated with latitude and/or with each other, including the possibility to display the results for all quantities

Table 3.1: Differences between the pulsar-only and the generalised Monte-Carlo technique.

between the *pulsar-only* and the *generalised* Monte-Carlo technique are summarised in table 3.1.

3.4 The results and error estimations

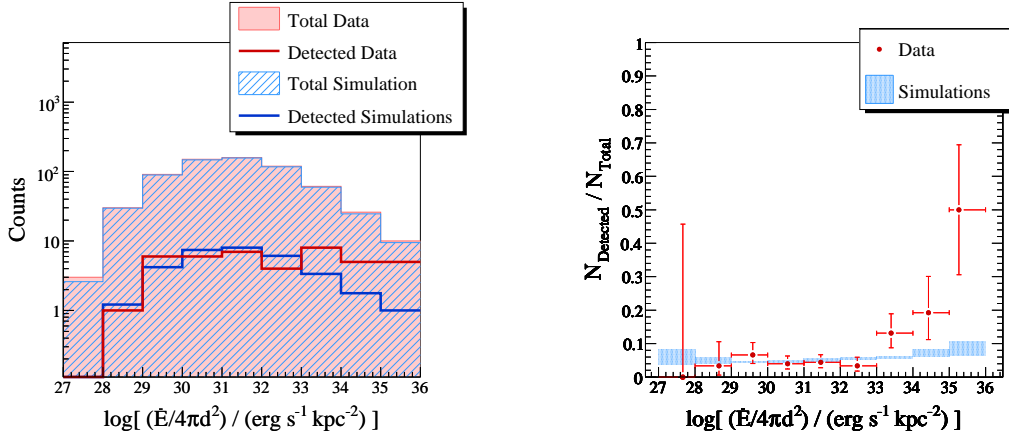


Figure 3.6: **Left:** The $\log[\dot{E}/4\pi d^2]$ distribution of all (filled areas) and detected (lines) PWNe. The data are shown in red and the MC results in blue. **Right:** The ratio of detected over all PWNe for the data (red) and the simulation (blue). The $\log[\dot{E}/4\pi d^2]$ -error bars show the width of each band, while the point shows the centre of gravity of the respective band.

Astrophysical objects are said to be detected in VHE γ -rays if the signal at the objects position exceeds 5σ above background in the H.E.S.S. significance map. For pulsar wind nebulae it is expected that the γ -ray emission is driven by the spin-down energy loss of the pulsar and that the observed flux depends on $1/4\pi d^2$. Therefore,

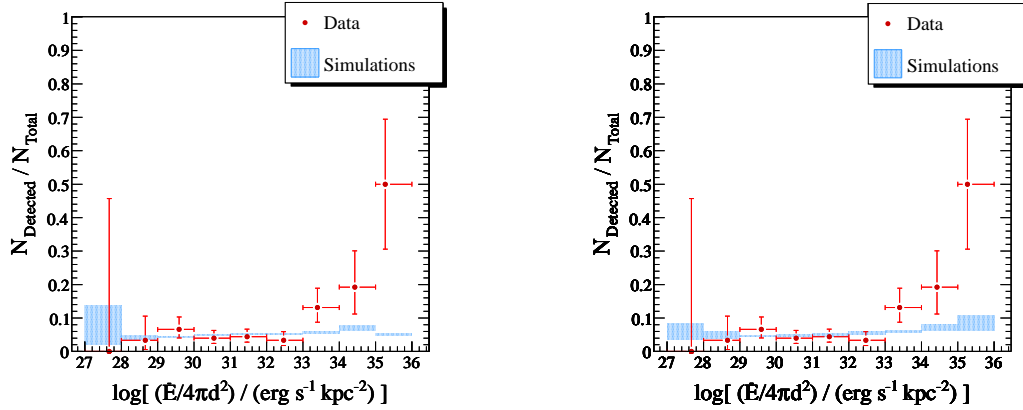


Figure 3.7: Comparison between the results for different estimations of the uncertainty in the Monte-Carlo. The ratio of detected over all PWNs for the data (red) and the simulation (blue) are shown. **Left:** The blue boxes in this panel are determined using the same method as by Carrigan [16], i.e. by simulating following the two parametrisations shown as blue dashed lines in Fig. 3.3. **Right:** Here, the blue boxes are determined from simulations where 9 ± 3 bands are used for the parametrisation of the width of the latitude distribution. It can be seen that the uncertainty from the different binning is larger than the uncertainty in the distribution itself, apart for the first bin in which the data has very low statistics.

the left panel of Fig. 3.6 shows the $\log[\dot{E}/4\pi d^2]$ distribution of all (filled areas) and detected (lines) pulsars for the data (red) as well as the simulations (blue), while the right panel of the same figure shows the ratio of detected over all PWNs for the data (red) and simulation (blue).

The error bars for the data are calculated using a *binomial confidence interval* method described below, while the blue boxes represent the uncertainty of modelling with different number of $\log[\dot{E}/4\pi d^2]$ -bands in the method describe above, i.e. 9 ± 3 bands for the PWNs. If more correlated quantities are used, the uncertainty (i.e. in the width of the distribution) is also included in the same way. Carrigan [16] estimated the uncertainty of the MC in a different way: by modelling the PWNs using parametrisations following the error bars in the right panel of Fig. 3.3 (blue dashed lines). In Fig. 3.7, the results of this method (left panel) are compared to the results of the method where the number of bins is varied (right panel). It can be seen that apart from the first bin the uncertainty from the different binning is larger than the uncertainty in the distribution itself.

The *binomial confidence interval* method used here is the same as Carrigan [16] applied and it is based on a paper by Clopper and Pearson [17]. Given a total number N of objects of which n are detected in VHE γ -rays and the real percentage p of objects to emit VHE γ -rays, the distribution of detectable objects is given by the

binomial distribution:

$$b(n, N, p) = \binom{N}{n} p^n (1 - p)^{N-n} . \quad (3.2)$$

For the error bars, the upper and lower boundary of the percentage p are searched for, in order to give a confidence interval with a confidence level $c = 68\%$. This can be written as:

$$\{ p \mid P[\text{Bin}(N, p) \geq n] \leq c/2 \} \cap \{ p \mid P[\text{Bin}(N, p) \leq n] \leq c/2 \} \quad (3.3)$$

where $\text{Bin}(N, p)$ is a binomial random variable with N trials and probability of success p . In other words, the asymmetric error bars for the fraction of detected objects give the 68% confidence range for the real percentage of objects emitting VHE γ -rays. For a more detailed and mathematical explanation see [16].

For the pulsars, the probability that the detection of VHE γ -rays from high-power pulsars (i.e. $\log[\dot{E}/4\pi d^2] > 35$) is caused by chance coincidence is $\sim 0.22\%$. For pulsars with $\log[\dot{E}/4\pi d^2] > 34$, the probability of chance coincidence is $\sim 0.094\%$. If a positive correlation is found, it does not necessary imply that the astrophysical objects in question emit the VHE γ -rays themselves. Some mechanisms related to the objects or their environment could be responsible for VHE γ -ray emission, for example if investigating the VHE γ -ray emission within HII or star forming regions, objects within these region might be the source of the emission, or vice-versa when investigating objects within those regions.

Chapter 4

Catalogues and Results

In this chapter, the astronomical objects and the motivation for the correlation study are presented. A brief description of the catalogues that are used is given and the results of the correlations studies are shown and discussed. Where required, the variation to the method (chapter 3) is also described.

Correlation studies have been performed with the following astrophysical objects: supernova remnants (section 4.1), star forming regions (section 4.2), HII regions (section 4.3), Galactic bubbles (section 4.4), OB stars and OB associations (section 4.5), Wolf-Rayet stars (section 4.6) and X-ray binaries (section 4.7).

4.1 Supernova remnants

At the end of their lives massive stars (i.e. $M \gtrsim 8M_{\odot}$) explode as supernovae. What remains are usually a neutron star or a black hole, and the supernova remnant (SNR, Fig. 4.1), which consists of an expanding shock wave, created by the ejected material interacting with the surrounding interstellar medium (ISM). Another possible scenario for supernova explosions and SNRs is when white dwarfs (compact objects supported by degenerate-electron pressure) accrete matter from a companion star and reach their critical mass. These supernovae are called type Ia supernova remnants, while the core-collapse supernovae described before are called type Ib, Ic or type II supernovae, depending on the spectral features of the supernova. Supernova remnants are usually first detected through radio observations sensitive to synchrotron emission in magnetic fields (see e.g. Green (2004) [42]), but are often visible in various wavelengths, from infrared to VHE γ -rays.

There are three types of SNRs: (a) shell type SNRs, where the emission comes from the outer part of the remnant, (b) composite SNRs, where a pulsar wind nebula (PWN) is found within the shell and (c) filled centre SNRs, in which central thermal X-ray emission is seen, enclosed by a radio shell.

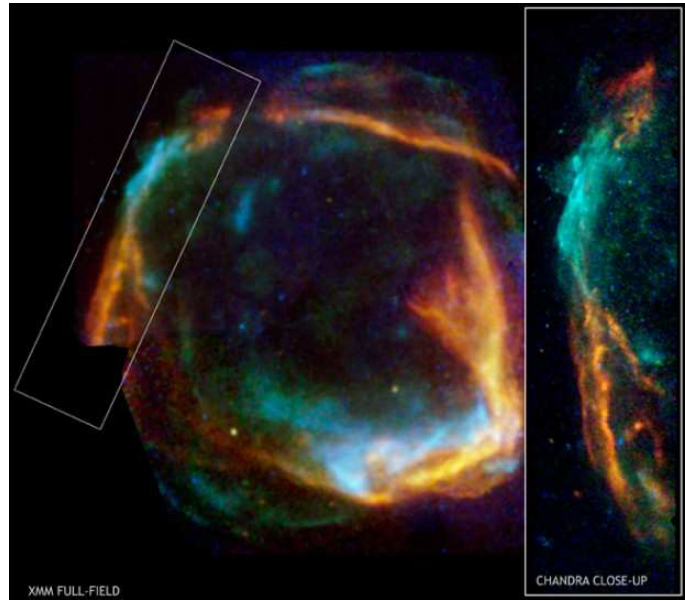


Figure 4.1: The combined image from the Chandra and XMM-Newton X-ray observatories of the supernova remnant RCW 86 shows the expanding ring of debris that was created after a massive star in the Milky Way collapsed onto itself and exploded. Both the Chandra and XMM images show low energy X-rays in red, medium energies in green and high energies in blue. The Chandra observations focused on the northeast (left-hand) side of RCW 86, and show that X-ray radiation is produced both by high-energy electrons accelerated in a magnetic field (blue) as well as heat from the blast itself (red). Scale: Chandra field of view is 38 arcmin across. Credit: Chandra: NASA/CXC/Univ. of Utrecht/J.Vink et al. XMM-Newton: ESA/Univ. of Utrecht/J.Vink et al.

4.1.1 Motivation

SNRs are commonly considered to be cosmic particle accelerators, up to energies around the “knee” in the cosmic ray spectrum, at $\sim 10^{15}$ eV, where the spectral index softens from $\Gamma \sim 2.7$ to 3.2 (see Fig. 1.1). This is supported by theory as well as by experiments. From theoretical considerations one can expect cosmic rays coming from shell type SNRs, where the particles are accelerated in shock waves through diffusive shocks (see section 2.1.2), as well as in plerions (pulsar wind nebulae), where the particles are accelerated in the terminal shock, between the relativistic outflow of electrons from the pulsar surface and the outer nebula. Furthermore, the Galactic supernovae and the resulting SNRs are the only known potential sources that can provide the necessary amount of energy (Ginzburg & Syrovatskii [41]).

A number of SNRs have already been observed in VHE γ -rays with various instruments before H.E.S.S., confirming that they are indeed sites of particle acceleration. The Whipple collaboration [37] reported the first detection of a SNR, the Crab Nebula, in 1989, however it is now known that the emission comes from a PWN and not the SNR itself. Since then, shell type SNRs were observed by different γ -ray detectors, e.g. Cas A by HEGRA [25] and RX J1713.7-3946 by the CANGAROO collaboration (Enomoto et al. [34]). H.E.S.S. has also detected some known or previously unknown VHE γ -ray SNRs, such as RX J1713.7-3946 and RCW86. Although the population of detected SNRs in VHE γ -rays is constantly increasing, previous observations have only provided a rather low level of emission compared to theoretical predictions [31], [45].

Because some SNR *are* sites of cosmic particle acceleration and in view of the puzzling deficit of VHE γ -ray detections, a correlation study of SNRs with H.E.S.S. data is performed in this work.

4.1.2 The catalogue

The catalogue used for the correlation study of supernova remnants with H.E.S.S. data is the well known SNR catalogue from Green [43]. The version of the catalogue from April 2006 is used and contains 265 SNRs (204 within the H.E.S.S. scan region), with basic information as well as comments and references for each SNR (see [43] for more details). The basic parameters of interest are the position, the radius, the flux density and the SNR type. The observed surface brightness of each SNR is computed via Eq. 3.1. Since the type (shell, composite or filled centre) is given, it is possible to investigate the shell type SNRs alone.

The catalogue is far from being homogeneous because of the different observation methods used to identify the SNRs. Some were identified from wide area surveys and others from smaller searches and different instruments, making uniform criteria for inclusion in the main catalogue difficult. Therefore some SNRs might be missing, while other sources could mistakenly be interpreted as being SNRs. Furthermore, the quality and certainty of some parameters varies, especially concerning the flux density.

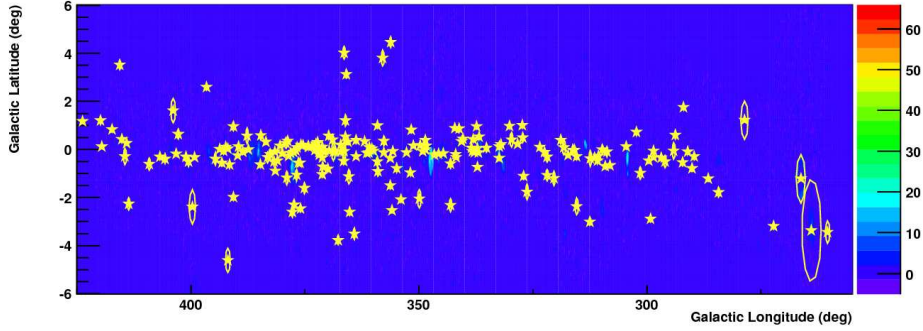


Figure 4.2: *H.E.S.S. significance map with the positions of supernova remnants from Green [43] superimposed. The stars mark the centre of the SNR while the circles (seen as ellipses because of the different scaling) represent the mean size of the remnants.*

It is interesting to discuss the influence of the selection effects, mainly those applicable at radio frequencies, because most SNRs were detected in this frequency range. The main difficulty lies in the identification of faint SNRs as well as of small and possibly bright SNRs. The surface brightness has to be high enough to distinguish the SNRs from the background. This selection bias is not uniform across the sky, because the background and the sensitivity of the instruments vary. Although fainter SNRs tend to be larger and therefore usually older, this selection effect also affects young remnants because even SNRs with known distances show a wide range of different properties, making a generalisation difficult. Because it is not easy to resolve the structure of small SNRs, they are also likely to be missed. This selection effect is more important for filled centre SNRs than for shell type SNRs, because even if they are large enough to be resolved, their centrally brightened structures may not be striking enough to be recognisable as filled-centre remnants. Furthermore young but distant SNRs seem to be missed with these surveys, see discussion in [42].

The consequence of these selection effects is that some SNRs which could be good candidates for VHE γ -ray emission, i.e. filled, plerionic and bright SNRs, might be missing. This could mean, that the catalogue is for our means “contaminated” with a relatively high proportion of uninteresting SNRs.

4.1.3 Distributions for the Monte-Carlo

Figure 4.2 shows a H.E.S.S. significance map, where the supernova remnants from Green’s catalogue within the H.E.S.S. scan region are superimposed (yellow stars, ellipses show the mean radius for very extended SNRs). The distributions of longitude, latitude, radius and flux density are shown in Fig. 4.3. For the Monte-Carlo, the longitude distribution is split into two bands, for radii smaller and greater than 15 arcmin respectively (Fig. 4.3(a)), because for greater radii the distribution is flat,

	Surface brightness $\log[F_{1\text{GHz}}/\text{Jy}]$	Detections out of #SNRs	Probability of chance coincidence
All SNRs	5.9 - 6.7	≥ 11 out of 56	0.37%
	6.7 - 7.5	≥ 4 out of 13	1.22%
	5.9 - 7.5	≥ 15 out of 69	0.02%
Shell type SNRs	5.9 - 6.7	≥ 7 out of 40	3.31%
	6.7 - 7.5	≥ 2 out of 7	8.59%
	5.9 - 7.5	≥ 9 out of 47	0.90%

Table 4.1: *The probabilities of chance coincidences for SNRs from [43] with VHE γ -ray signals. See text for a discussion of these results.*

while for smaller radii a third order polynom can be fitted. Once a radius is picked randomly from the fit to the radius distribution (see Fig. 4.3(c)), a random value for the longitude is determined from Fig. 4.3(a) and a value for the latitude and flux density are picked from the corresponding fits to the distributions in Figs. 4.3(b) and 4.3(d) respectively. The surface brightness is then determined from Eq. 3.1.

There are 161 supernova remnants from Green’s catalogue within the scan region which are classified as shell type or probably shell type SNRs. The remaining 43 SNRs are either classified as composite, filled centre SNRs or are unclassified. Shell type SNRs are more interesting for this correlation study, since plerions (composite or filled centre SNRs) are ideally already considered in the PWN correlation study. Therefore the catalogue is divided into two classes: shell type SNRs and the rest. To model the shell type SNRs only the distributions of shell type SNRs are used (see Fig. 4.3(b-d)). Because of the low statistics the rest of the SNRs are modelled using the distributions of the whole catalogue. The radius-latitude correlation is also modelled using the data of the whole catalogue in order to achieve better statistics.

4.1.4 Results

The maximal significance within each SNR’s extend is searched for in a significance map with a correlation radius $\theta = 0.1^\circ$ for point-like sources, in order to find VHE emission, possibly coming from the shell. If the significance exceeds 5σ , then the SNR is said to be detected. The results after simulating $5 \cdot 10^5$ samples of supernova remnants are shown in Fig. 4.4. A trend can be seen: SNRs with higher surface brightness seem to be detected more often, which would be reasonable. However, the uncertainty is quite high due to the low statistics.

The probabilities of chance coincidences for SNRs with a surface brightness falling into the third and fourth bins in Fig. 4.4 are summarised in table 4.1. The lower probabilities of chance coincidence for all SNRs show that the SNRs classified as composite, filled centre or of unknown type seem to play a significant role in the detection of VHE γ -rays coming from SNRs. It is reasonable to assume that plerions

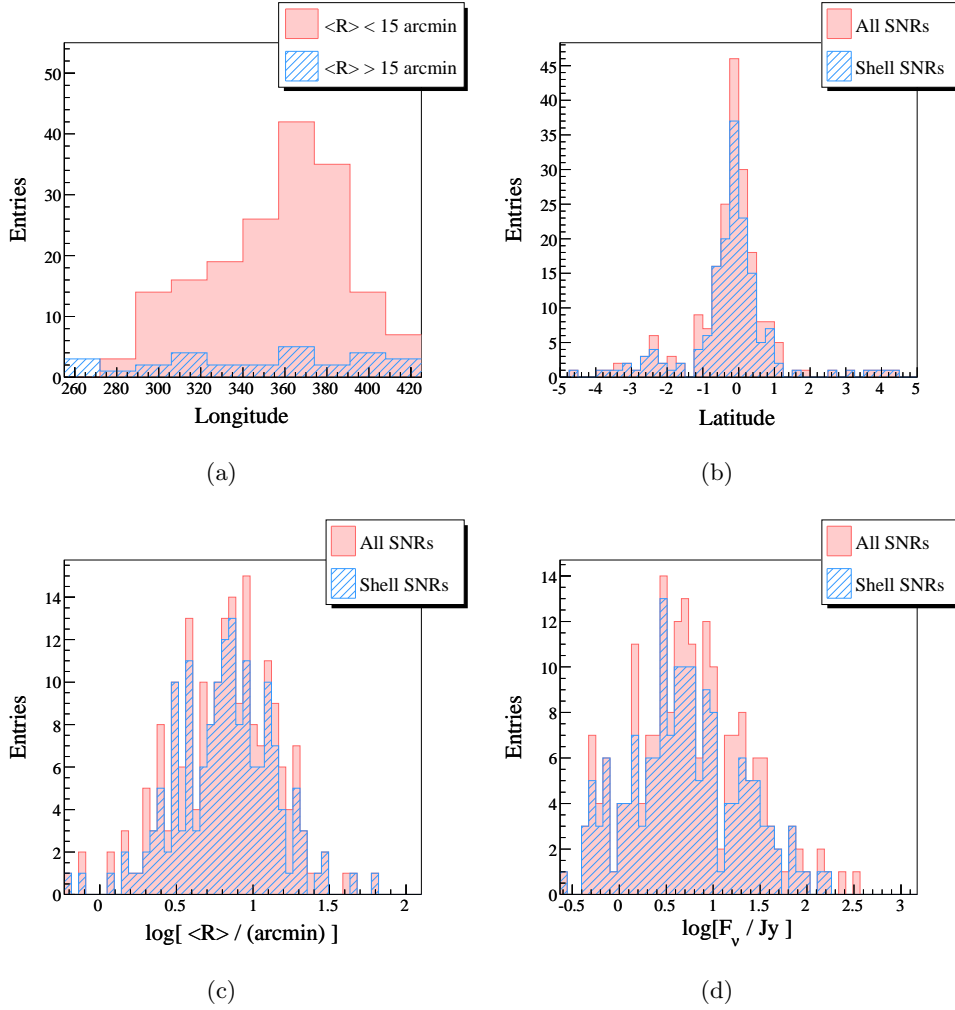


Figure 4.3: The distributions of the Galactic longitude, Galactic latitude, mean radius and flux density of the supernova remnants from [43]. The longitude distribution is divided into SNRs with a mean radius smaller and greater than 15 arcmin respectively. For the other distributions, the component coming from the shell type SNRs is shown as a blue hashed area.

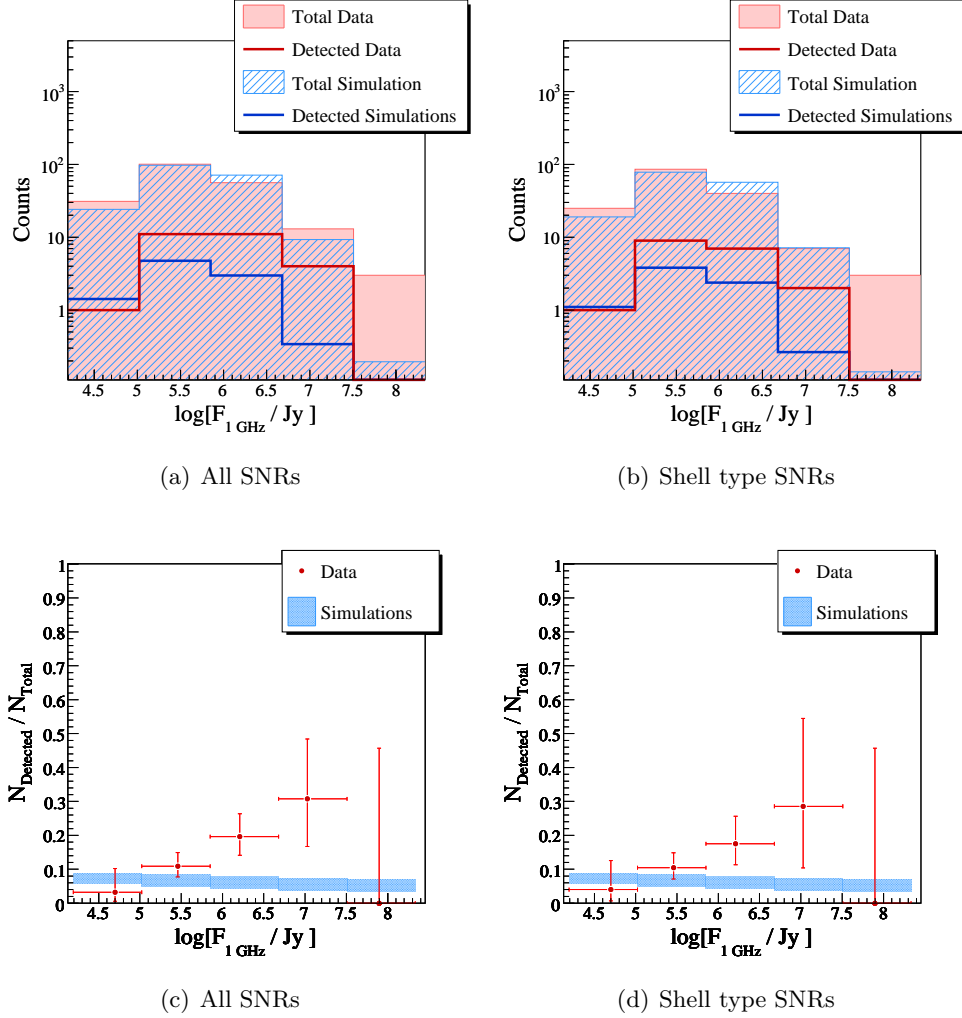


Figure 4.4: The results of the correlation study of the supernova remnants from [43] with H.E.S.S. data. **(a)** Distribution of all (filled areas) and detected (lines) SNRs for the data (red) and the simulation (blue) as a function of the surface brightness, for all the SNRs within the H.E.S.S. scan region. **(b)** Distribution of all (filled areas) and detected (lines) SNRs for the data (red) and the simulation (blue) as a function of the surface brightness, for the shell type SNRs within the H.E.S.S. scan region. **(c)** Ratio of detected over all SNRs for the data (red) and simulations (blue) as a function of the surface brightness, for all the SNRs within the H.E.S.S. scan region. **(d)** Ratio of detected over all SNRs for the data (red) and simulations (blue) as a function of the surface brightness, for the shell type SNRs within the H.E.S.S. scan region. See text for a discussion of these results.

(i.e. PWN) embedded in SNRs are responsible for part of this emission. On the other hand, the lower statistics are also responsible for the greater uncertainties for the shell type SNR results.

It is interesting to have a look at the results of the same study as a function of the mean radius in Fig. 4.5. For radii greater than ~ 15 arcmin ($\log[\langle R \rangle] \approx 1.2$) the ratio of detected SNRs strongly increases since with large search radii, the probability of finding a VHE γ -ray signal dramatically increases. The detected SNRs from the simulations increase steadily with greater radii as expected.

4.1.5 The supernova remnant G327.1-1.1

In the scope of correlation study of supernova remnants with H.E.S.S. data, a hot spot coincident with the supernova remnant G327.1-1.1 was found.

G327.1-1.1 is a composite supernova remnant similar to W44, with a shell seen in radio and a pulsar wind nebula seen in radio and X-rays. The age of the SNR is estimated to be 11000 yr by Sun et al. [61] or up to more than 30000 yr if the SNR is assumed to be in the radiative expansion phase (i.e. the first cooling phase after the sweeping up of the interstellar medium) (Bocchino et al. [14]), its angular size is about 17.5 arcmin and its distance is estimated to be 9 kpc [61]. As with W44, the X-ray emission is the sum of a non-thermal component, due to the PWN and the pulsar itself, and of a fainter thermal component. Unlike many other SNRs, their thermal X-ray component peaks at the centre. The X-ray photon index of the power-law component is $\Gamma \sim 2.2$ [61]. The plerionic component is, like W44, at an offset from the centre of the shell and it elongates in the southeast-northwest direction (Fig. 4.6). Chandra observations (see Fig. 4.7) have confirmed the presence of a compact source at the northwestern end of the elongation, supporting the theory of a moving pulsar leaving a trail as it moves out of the boundary of the plerionic structure, as proposed in [61].

H.E.S.S. observations

In the correlation study G327.1-1.1 was detected with an excess slightly above 5σ . However, it only appears as a source if hard cuts and a Θ^2 for point-like sources are used, which was the case in the correlation study. The observation lifetime for G327.1-1.1 is about 14 hr, giving an acceptance corrected observation time of about 6 hr. This is because the data comes from the Galactic scan only, which results in generally high pointing offsets, lying in half of the cases above 2° .

Figure 4.6 shows a Molonglo Observatory Synthesis Telescope (MOST) 843 MHz radio image of G327.1-1.1 with contours of the H.E.S.S. data (white) and the Chandra public data from the HEASARC web page [2] (black). The position and size as measured by BeppoSAX [14] is also shown (cyan circle). The green dashed circle represents the uncertainty of the position of the H.E.S.S. source. The H.E.S.S. fit position is R.A. 238.655° , decl. -55.052° (J2000) with an uncertainty of $\pm 0.025^\circ$ and the fit size is consistent with a point-like source.

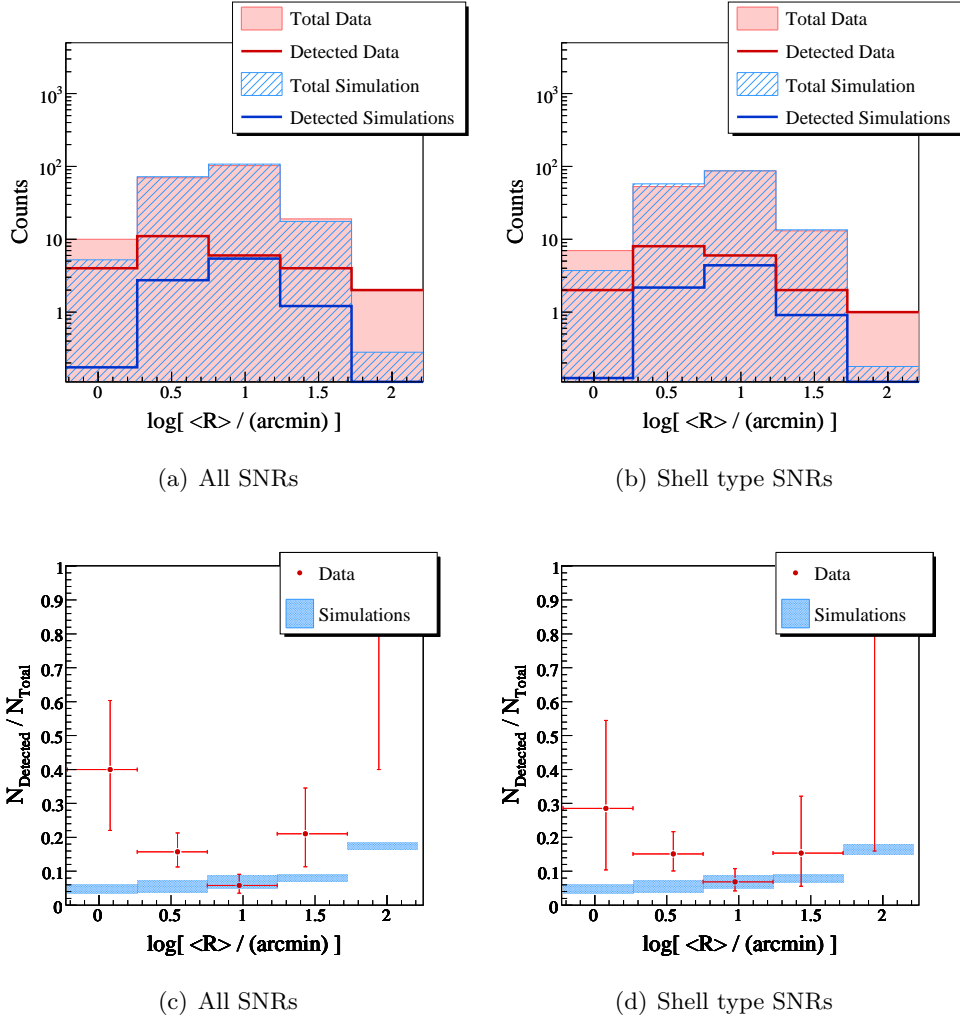


Figure 4.5: The results of the correlation study of the supernova remnants from [43] with H.E.S.S. data as a function of the mean radius. (a) Distribution of all (filled areas) and detected (lines) SNRs for the data (red) and the simulation (blue) as a function of the mean radius, for all the SNRs within the H.E.S.S. scan region. (b) Distribution of all (filled areas) and detected (lines) SNRs for the data (red) and the simulation (blue) as a function of the mean radius, for the shell type SNRs within the H.E.S.S. scan region. (c) Ratio of detected over all SNRs for the data (red) and simulations (blue) as a function of the mean radius, for all the SNRs within the H.E.S.S. scan region. (d) Ratio of detected over all SNRs for the data (red) and simulations (blue) as a function of the mean radius, for the shell type SNRs within the H.E.S.S. scan region. See text for a discussion of these results.

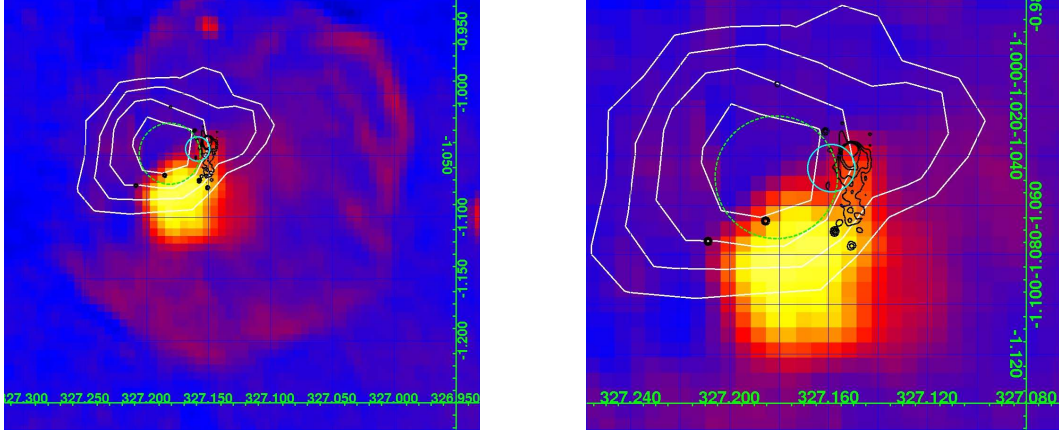


Figure 4.6: The MOST 843 MHz radio image of G327.1-1.1 (**left:** plerion + shell, **right:** plerion) in galactic coordinates with in white the contours of the H.E.S.S. data (showing 3, 3.5, 4, 4.5 σ respectively) and in black the Chandra data. The position and size as measured by BeppoSAX is also shown (cyan circle). The green dashed circle represents uncertainty of the position of the H.E.S.S. source.

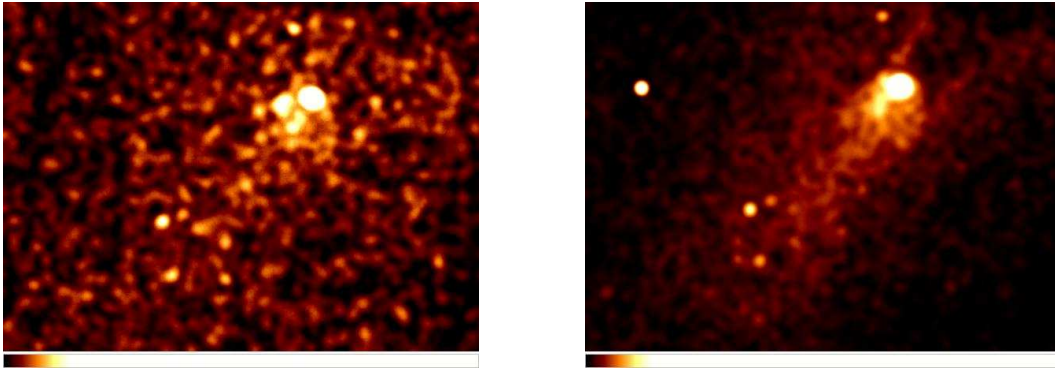


Figure 4.7: Chandra images of the probable pulsar in G327.1-1.1. (**left:** above 5 keV, **right:** below 5 keV), shown in equatorial (J2000) coordinates and therefore rotated with respect to Fig. 4.6. There is a hint of shrinking for lower energies towards the bright spot which could be the pulsar.

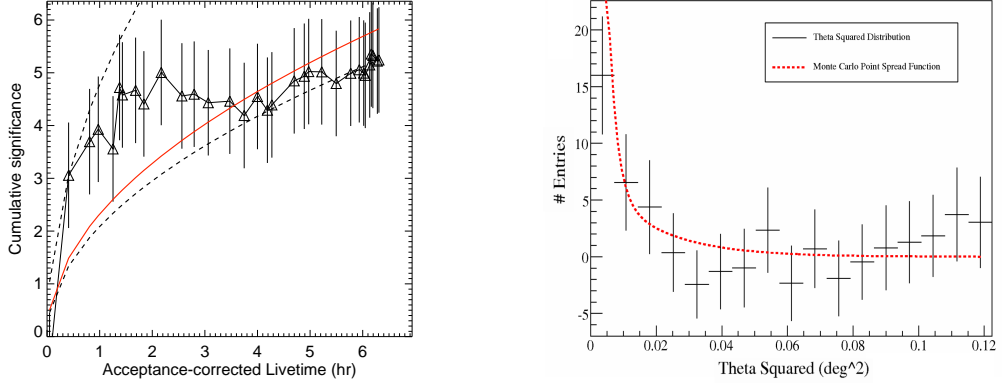


Figure 4.8: **Left:** The significance as a function of the acceptance corrected observation time t . The red line shows the best fit, while the upper dashed line shows the \sqrt{t} -law scaled to the first point above 3σ and the upper dashed line shows the \sqrt{t} -law scaled to the last point. **Right:** The excess in function of Θ^2 , confirming the point-like character of the source.

The first results of a Wobble Chain analysis are shown in Figs. 4.8. The left panel shows the excess as a function of the acceptance corrected observation time while in the right panel the excess in function of Θ^2 is shown, confirming the point-like character of the source. Looking at the left panel of Fig. 4.8 it is expected that with some more (dedicated) observation time, the source will be seen more clearly. With the available data so far, no spectrum could be extracted.

Technical feasibility

The almost unique characteristics of G327.1-1.1 in X-rays make it an interesting SNR. Being similar to W44, for which only about 4σ after 35 hr of observations with H.E.S.S. are obtained (see the H.E.S.S. source catalogue [1]), enables the comparison between those two SNRs and might give some new insights concerning the physics of these two composite SNRs. Because of the small amount of observations so far and the large mean offset of the available data, additional dedicated observations were requested. Unfortunately, due to sharing the same RA-band as SN1006, this observation time will be granted at the earliest in spring 2009.

Assuming an excess of 5σ within 6 hr of observation, more than 8σ are expected with an additional 10 hr. This would allow to define the source's position and extent more precisely and to extract a spectrum. Moreover, together with the available multi-wavelength data from radio to X-rays, it could then be possible to constrain the nature of this source.

4.2 Star forming regions

Star forming regions (SFRs) are very active sites in the Galaxy and are the birth place of young stars. They are usually found in the Galactic spiral arms, where the high density of material makes the collapse of giant molecular clouds onto themselves possible. There are several scenarios leading to the collapse of a giant molecular cloud. Either it is so massive that the gas pressure is not high enough to support the cloud against gravitational collapse or the cloud is compressed by events such as supernova explosions, collisions of molecular clouds or even collisions of galaxies, enabling the gravitational collapse. The second scenario is called triggered star formation. A prominent star forming region is shown in Fig. 4.9.

Star forming regions contain a variety of objects such as young (proto-)stars, HII regions, bubbles, etc. Some objects related to star forming regions will be treated separately later on in this work.

4.2.1 Motivation

There are several potential mechanisms by which VHE γ -rays could be emitted within star forming regions. Possible contributions could come from shock fronts created by colliding stellar winds [57], second order Fermi acceleration within molecular clouds (section 2.1.2) or jets coming from protostars [9]. Lately, effort has been invested into describing the last mechanism. Although Araudo et al. [9] claim that VHE γ -rays should be emitted by protostellar jets, the flux is probably too low to be detected by present experiments. Nevertheless, a correlation study may provide some useful informations.

Belotsky et al. [11] have performed a correlation study between regions of star formation (RSF, from Avedisova [10]) and unidentified high energy (50 MeV - 5 GeV)¹ γ -ray sources (UGS) within 5° in latitude from the Galactic equator. Of the 40 UGSs with Energies above 100 MeV, 19 (i.e. $47 \pm 8\%$) coincide positionally with regions of star formation from [10]. Therefore they consider RSF meaningful candidates for the clarification of UGS, but emphasise that the statistics are too low for decisive conclusions. In this work, the same catalogue is compared to H.E.S.S. data.

4.2.2 The catalogues

There are two catalogues which were used in the correlation study of star forming regions with H.E.S.S. data. The first catalogue is from D. Russeil [59] and contains 307 star forming complexes. The other catalogue is the catalogue of star forming regions from Avedisova [10] used by Belotsky et al. in their correlation study. This catalogue is a compilation of data from about 3300 regions of star formation, coming from various observations. In the following the two catalogues are treated separately.

¹From observations with the space stations COS-B, GRO-COMPTON (NASA) and GAMMA (Roskosmos) in the period 1980-2000



Figure 4.9: *The Orion nebula, the massive star forming region closest to Earth containing probably about 1000 young stars. This image is a false-colour composite with data coming from NASA's Spitzer and Hubble Space Telescopes. The image covers approximately the apparent angular size of the moon. Light detected at wavelengths of 0.43, 0.50 and 0.53 microns is blue, light with wavelengths of 0.6, 0.65 and 0.91 microns green, while light of 3.6 microns is orange, and 8-micron light is red. The swirls of green are hydrogen and sulfur gases heated by intense ultraviolet radiation from stars. Wisps of red indicate infrared light from illuminated clouds containing carbon-rich molecules called polycyclic aromatic hydrocarbons. Spitzer exposed infant stars deeply embedded in a cocoon of dust and gas (orange-yellow dots). Hubble found less embedded stars (specks of green) and stars in the foreground (blue). The ridges and cavities were blown by stellar winds from clusters of newborn stars scattered throughout the cloud. (Image from [53]).*

4.2.3 Catalogue I: Distributions and Monte-Carlo

Russeil [59] has grouped different young Galactic objects into star forming complexes in order to investigate the spiral structure and kinematics of our Galaxy. This grouping eliminates the ‘noise’ due to spatial and kinematic dispersion of the sources, thereby constraining the systemic velocity and stellar distance and decreasing any spatial and velocity scattering and mixing. Several ionised and molecular sources are grouped based on kinematic and spatial considerations. A complex can either contain HII regions and ionised patches, or HII regions, ionised patches and molecular clouds or molecular clouds alone. However, molecular clouds alone are not massive star forming complexes, but they may contain star forming sites with no HII region detectable yet.

The catalogue contains information about the position, the systemic velocity, the kinematic distance, the stellar distance and an excitation parameter. The excitation parameter quantifies the activity of each complex (in pc cm^{-2}). It is a direct measure of the ionising photons produced and is determined from the radio continuum flux (see Schraml & Mezger [60]). The excitation parameter of the complexes is calculated using the excitation parameter of the individual sources, but many of these sources do not have radio continuum measurements, resulting in an underestimated excitation parameter for the star forming complexes. Russeil estimates the catalogue to be complete for complexes brighter than 60 pc cm^{-2} (see Fig. 4.10 for the distribution of the excitation parameter).

There are 307 star forming complexes from [59] within the H.E.S.S. scan region. The distributions of their longitude, latitude, excitation parameter as well as the correlation between the latitude and the excitation parameter are shown in Fig. 4.10. The modelling of this catalogue does not differ much from the basic method used for the pulsar wind nebulae, since no extra quantity, no special correlation and no further classification is found.

4.2.4 Catalogue I: Results

The H.E.S.S. significance map used to derive the significance of the VHE γ -ray signals at the star forming complexes’ positions has a correlation radius $\theta = 0.22^\circ$, since several smaller regions are grouped together. The results are shown in Fig. 4.11. The probability of chance coincidence for SFCs with an excitation parameter greater than about 300 (3 or more out of 5) with H.E.S.S. sources is $\sim 0.63\%$. For SFCs with an excitation parameter greater than about 150 it is $\sim 0.65\%$.

The results show that although the statistics remain too low for decisive conclusions, a meaningful amount of SFCs coincide with VHE γ -ray sources. Furthermore there seems to be a trend, that SFCs with a high excitation parameter can more often be associated with a VHE γ -ray source. This is reasonable since the excitation parameter is a measure of the flux and the activity of SFCs.

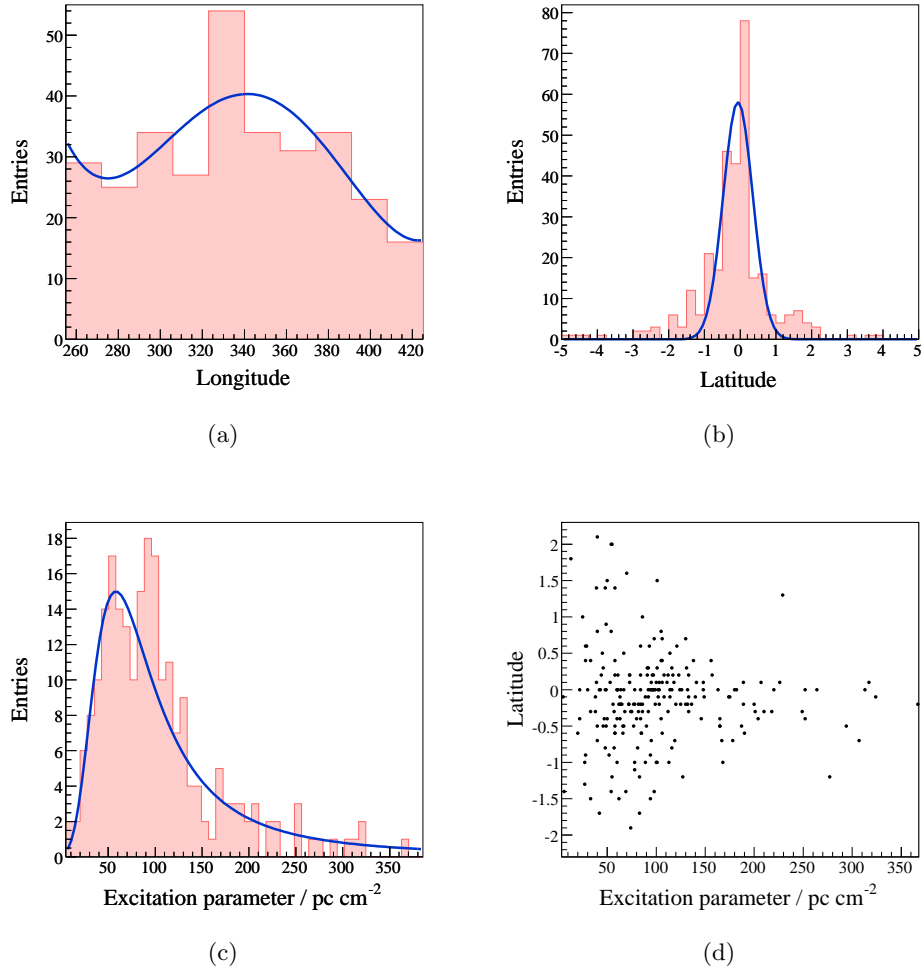


Figure 4.10: *The distributions of the Galactic longitude, Galactic latitude and excitation parameter of the star forming complexes from [59].*

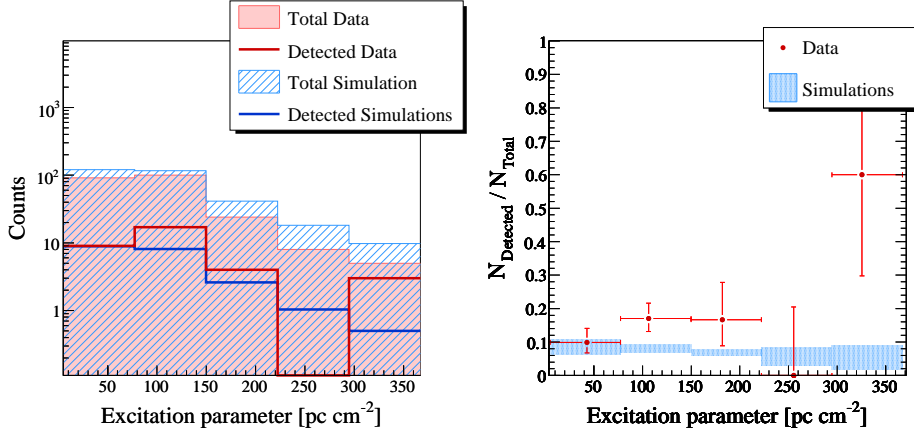


Figure 4.11: The results of the correlation study of the star forming complexes from [59] with H.E.S.S. data. **Left** Distribution of all (filled areas) and detected (lines) SFCs for the data (red) and the simulation (blue) as a function of the excitation parameter, for all the SFCs within the H.E.S.S. scan region. **Right** Ratio of detected over all SFCs for the data (red) and simulations (blue) as a function of the excitation parameter. See text for a discussion of these results.

4.2.5 Catalogue II: Distributions

As opposed to Russeil [59] who grouped young sources into complexes, Avedisova [10] provides a catalogue of individual sources. The catalogue contains about 3300 (possible) regions of star formation (RSF), with over 66500 entries from different references containing information about the regions. 2603 sources out of the 3229 sources within the H.E.S.S. scan region are RSF (the other sources lack velocity data and are therefore only RSF candidates). The RSF can be divided into several subtypes, depending on the type of information present in the catalogue within each region (explained in table 4.2). Each RSF can be described as a set of these classes. The classes RIM, IM and ORIM are the only classes statistically relevant for the correlation study. The different classes show different distributions on the sky (see Fig. 4.12). The distribution of RIM objects (Fig. 4.12(a)) is characteristic of RSF in which massive stars are formed, while the lack of optical data indicates large distances. Classes with available optical and radio data (Fig. 4.12(c) and (g)) are probably close to the sun. The distribution of IM objects (Fig. 4.12(b)) is similar to the overall distribution, suggesting that these objects are not a homogeneous class and represent a mixture of high and low mass RSF. For a more detailed discussion about the different classes see [10].

Unfortunately, for most sources there are a number of different values for several parameters coming from various observations over the last few decades. The catalogue was sorted following the description given by Avedisova [10]. The data available on the size of the sources is very limited, especially for the classes of interest

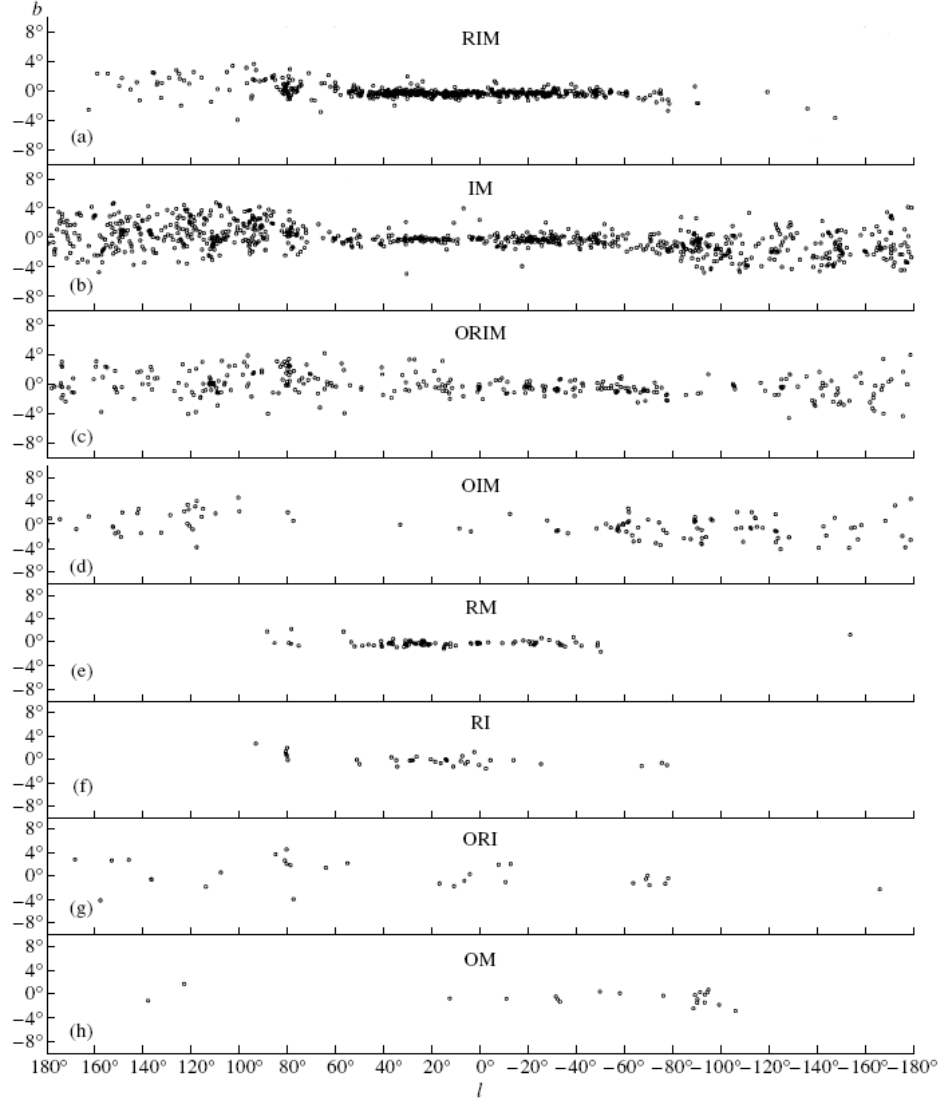


Figure 4.12: The distributions of the different classes of RSF from [10]. See table 4.2 for the description of the individual letters representing the type of data or objects found within the sources. The different distributions reflect the properties of different sorts of objects. The distribution of RIM objects (Fig. 4.12(a)) is characteristic of RSF where massive stars are formed, while the lack of optical data indicates large distances. Classes with available optical and radio data (Fig. 4.12(c) and (g)) are probably close to the sun. The distribution of IM objects (Fig. 4.12(b)) is similar to the overall distribution, suggesting that these objects are not a homogeneous class and represent a mixture of high and low mass RSF. See [10] for a more detailed explanation. (Image from [10])

D	dark clouds and globules
O	optical objects (stars, diffuse and reflection nebulae, Herbig-Haro objects)
I	infrared objects (accretion disks, cocoons, dense cores of molecular clouds)
R	radio objects (HII regions)
M	molecular composition of the circumstellar gas around stars, masers

Table 4.2: *The classification of the sources in [10] and the type of data or objects found within the sources.*

with a significant amount of sources (RIM, IM, ORIM). Furthermore the information given on the flux density is frequency dependent, which varies from observation to observation. Other information given in the catalogue is also not useful for a Monte-Carlo simulation, therefore only the detections in a H.E.S.S. significance map with a correlation radius $\theta = 0.22^\circ$ are determined, neglecting possible dependences on any physical quantity.

4.2.6 Catalogue II: Results

The number of regions of star formation with a VHE γ -ray significance $\geq 5\sigma$ and the resulting probabilities of chance coincidence are shown in table 4.3. It seems that only RIM type RSF correlate significantly with VHE γ -ray signals. It is however surprising that the ORIM class RSF have a much higher probability of chance coincidence (56.7 %), since they are assumed to be the same kind of objects, only closer to the sun. This might be a reflection of the lower statistics, or that this class is not as homogeneous as thought. The probabilities of chance coincidences of the IM class are high which is in reasonable if it is assumed that they are a mixture of high and low mass RSF, where only high mass RSF would be correlated with VHE γ -ray emission. The probabilities of chance coincidences of all RSF and all sources in the catalogue seem to reflect the fact, that a considerable portion of RSF might be correlated with VHE γ -ray emission (i.e. the RIM class), while the rest does not correlate significantly or is not homogeneous enough to narrow down further possible classes correlating with VHE γ -ray emission.

4.3 HII regions

HII regions are clouds containing glowing gas and young hot blue stars (e.g. OB stars, section 4.5). These young stars emit considerable amounts of UV radiation which ionises the nebulae in which they are embedded, making the HII regions visible, sometime even to the naked eye. HII regions are formed in giant molecular clouds, after the hot stars needed for the ionisation are born (see SFR, section 4.2). The lifetime of HII regions depends on the radiation pressure of these stars, by which the surrounding gas will be driven away. A portion of the gas will eventually also

Class of object	Detections out of #RSF	Probability of chance coincidence
All sources	190 out of 1925	0.042 %
All RSF	151 out of 1465	0.025 %
RIM	90 out of 574	0.000079 %
IM	26 out of 340	20.1 %
ORIM	7 out of 145	56.7 %

Table 4.3: *The amount of detected RSF sources in the different classes from [10]. Note that there are more detections than H.E.S.S. sources, which means that multiple counting occurs. The RSF in the catalogue are somewhat clumped, which is not correctly reproduced by the Monte-Carlo, and might affect the probabilities of chance coincidence.*

be driven away by supernova remnants.

Their connection with star forming regions is useful to collect information about the stages of star formation. Since they are found within the spiral arms of the Galaxy and because they are observable in radio wavelengths which are not affected by dust extinction, they are very useful to probe distant parts of the Galaxy and to investigate its spiral structure.

4.3.1 Motivation

HII regions are associated with regions of star formation, i.e. regions which seem to be correlated with VHE γ -ray emission (see section 4.2). Since a number of different objects can be found in star forming regions, correlation studies of these individual objects might give some insight on the origin of the VHE γ -rays.

Possible Cosmic Ray (CR) emission connected to HII regions is discussed e.g. by Montmerle and Cesarsky [52]. They propose CR confinement by resonant Alfvén waves² and γ -ray emission in HII regions. In their idealised model of a region of star formation, CR are accelerated by stellar winds with their terminal shock front in HII regions. The stellar wind boundary separates the shocked region from the denser part of the HII region. The particles accelerated in the shocked region (see section 2.1.2) will experience resonant Alfvén wave scattering in the HII region, resulting in the confinement of the CRs. The confinement of CR protons and electrons is needed to enable the passing back and forth through the shock front of the CRs and the resulting acceleration, as well as for CR-collisions creating γ -rays.

²Alfvén waves are travelling oscillations of ions and magnetic fields in a plasma.

4.3.2 The catalogue

Paladini et al. [36] provide a radio catalogue of galactic HII regions. It contains 1442 Galactic HII regions organised in a master catalogue with the original data at different wavelengths, as well as a “synthetic” catalogue of fluxes and diameters at 2.7 GHz, a frequency for which the information is not complete but extensive and which lies in the middle of the frequency range, making an extrapolation from other wavelengths relatively reliable. In this correlation study the synthetic catalogue is used. It contains the position, flux density and the diameter for each HII region, supplemented by velocity data where available. The surface brightness is computed (Eq. 3.1) which becomes the main parameter, as for the SNR (see section 4.1).

To compile the catalogue 24 radio catalogues were used, where the HII regions are classified following Lockman et al [49] and only diffuse and compact HII regions were included. Paladini et al. emphasise the possibility that the catalogue may in principle contain some Galactic sources which are not HII regions. They therefore compared the HII regions with Green’s catalogue of SNR of 2000. However, some HII regions may have been identified as SNRs since then. A new comparison has not been performed yet. The selection effects are similar to those of the SNRs.

4.3.3 Distributions and Monte-Carlo

Of the 1442 Galactic HII regions in the catalogue, 1119 are found in the H.E.S.S. scan region. Figure 4.13 shows the distribution of the Galactic longitude and latitude, as well as the distribution of the mean radius and flux density. There is no division into classes or types.

For the modelling of the HII regions catalogue, the correlation between the mean radius and the latitude and the flux density respectively has to be taken into account. Since there are no further specific correlations and only one class of objects is present, there are no deviations from the method described in chapter 3.

4.3.4 Results

Since the HII regions found in the catalogue are diffuse or compact sources, a significance map with a correlation radius similar to the HII region’s radius is chosen for each HII region from a set of significance maps with several correlation radii. The results of $1.5 \cdot 10^5$ simulations are shown in Fig. 4.14 and the probabilities of chance coincidence are summarised in table 4.4.

HII regions from the data with surface brightnesses between $\log[F_{2.7\text{GHz}}/\text{Jy}] = 6.2$ and 7.9 seem to be detected slightly more often than the Monte-Carlo HII regions in that range. However, the probabilities of chance coincidences are rather high, although the statistics are relatively good. This suggests that some HII regions may indeed be correlated with VHE γ -ray emission, but that a further division in some subtypes with specific characteristics is necessary. This could permit to narrow down the possibilities of contributions to the VHE γ -ray emission of HII regions.

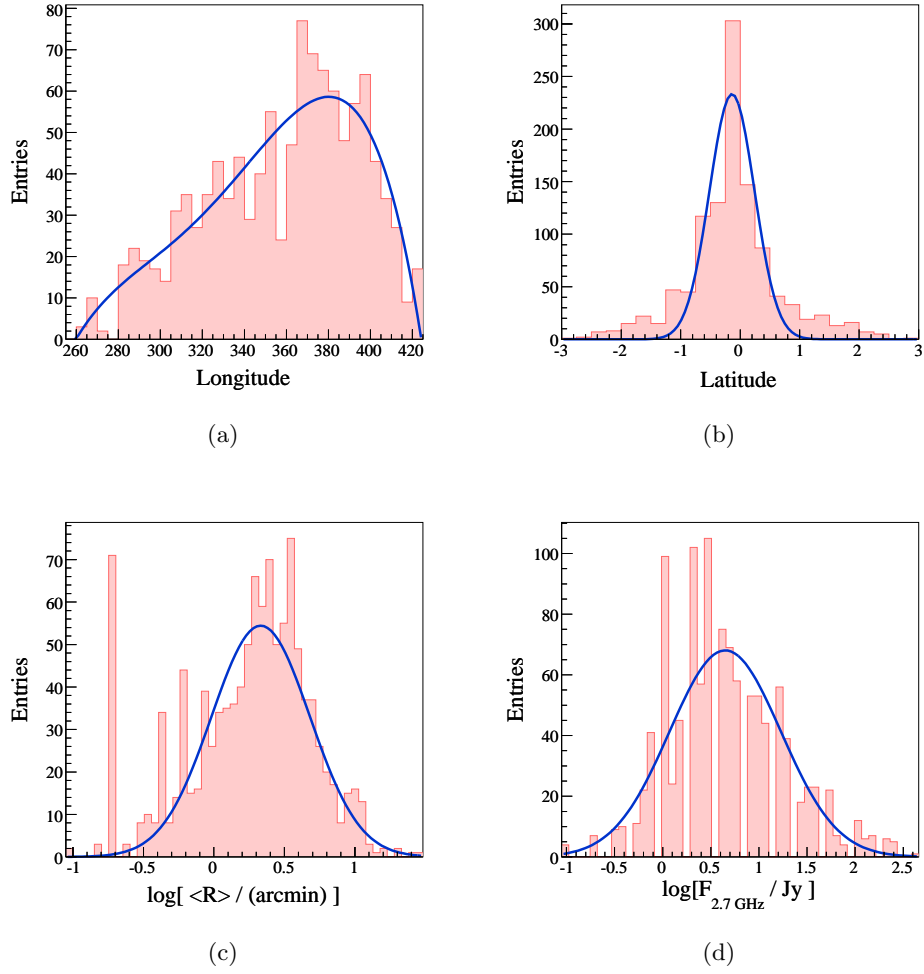


Figure 4.13: The distributions of the Galactic longitude, Galactic latitude, mean radius and flux density of the HII regions from [36].

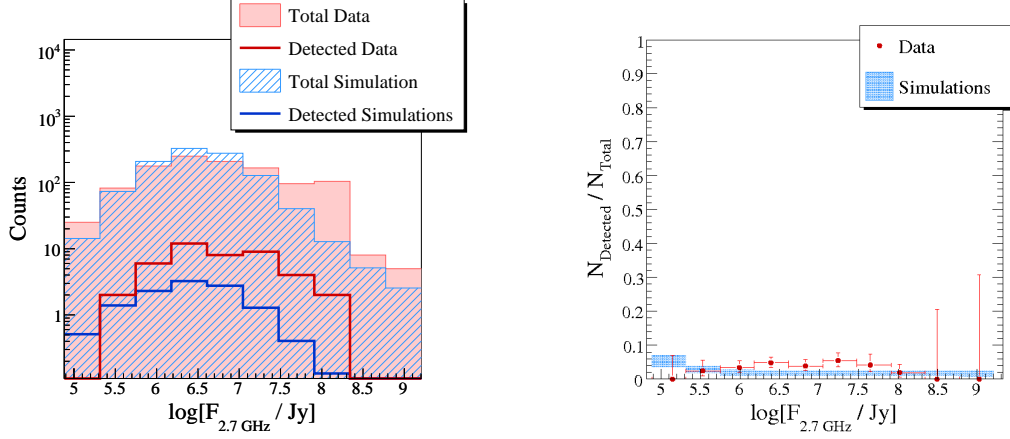


Figure 4.14: The results of the correlation study of the HII regions from [36] with H.E.S.S. data as a function of the surface brightness. **Left:** Distribution of all (filled) and detected (line) HII regions for the data (red) and the simulation (blue) as a function of the surface brightness, for all the HII regions within the H.E.S.S. scan region. **Right:** Ratio of detected over all HII regions for the data (red) and simulations (blue) as a function of the surface brightness, for all the HII regions within the H.E.S.S. scan region.

	Surface brightness $\log[F_{2.7\text{GHz}}/\text{Jy}]$	Detections out of #HII regions	Probability of chance coincidence
Single bins	6.2 - 6.6	≥ 12 out of 249	2.32%
	6.6 - 7.0	≥ 8 out of 207	14.3%
	7.0 - 7.5	≥ 9 out of 166	2.38%
	7.5 - 7.9	≥ 4 out of 96	21.3%
Several bins	6.2 - 7.5	≥ 29 out of 722	0.92%
	6.2 - 7.9	≥ 33 out of 818	0.55%

Table 4.4: The probabilities of chance coincidences for HII regions from [36] with VHE γ -ray signals. See text for a discussion of these results.

4.4 Galactic bubbles

When looking at the Galactic plane in infrared (e.g. with the Galactic Legacy Infrared Mid-Plane Survey Extraordinaire - GLIMPSE [30]) some partial and closed rings can be seen (Fig. 4.15). Churchwell et al. [32], [33] argue that these rings are partial or fully enclosed three dimensional bubbles, formed by hot young stars in massive star formation regions. The bubbles are small, generally a few arc-minutes in diameter.

The study of Galactic bubbles can give information about the stellar winds that produce them, the structure of the ambient interstellar medium in which they expand, as well as their impact on the magnetic fields in the ISM. They can also provide further understanding of triggered star formation processes, since some bubbles have morphologies suggestive of triggered or stimulated star formation.

4.4.1 Motivation

As mentioned above, bubbles are formed in star forming regions. Furthermore, about 25% of the bubbles coincide with known HII regions - the other 75% appear to be formed by late-B stars, whose ultraviolet radiation is not strong enough to ionise the surrounding ISM. Since these are two candidates for VHE γ -ray emission, it is interesting to search for correlations between the bubbles and H.E.S.S. data. However, there is no obvious possible acceleration mechanism proposed for Galactic bubbles. One could argue, that the strong stellar winds and the high density at the edge of the bubble might cause a termination shock. Because VHE energy γ -ray emission is not immediately expected, the correlation study with bubbles can be used as a tool to test the method.

4.4.2 The catalogue

Our catalogue for Galactic bubbles is a merger of two catalogues provided by Churchwell et al. [32], [33]. The first catalogue (CatI) contains 322 bubbles with longitudes $10^\circ < |l| < 65^\circ$, while the second catalogue (CatII) contains 269 bubbles within 10° of the Galactic centre, thus the region left out of the first catalogue.

The GLIMPSE false colour image mosaics (Fig. 4.15) were searched visually for bubbles by Churchwell et al. (see [32], [33] for discussions on the observer-dependent selection effects). The search criteria were different for the two catalogues, resulting in some differences in the distributions, especially for the size distribution, since the region of CatII was more thoroughly searched for small bubbles due to the higher background luminosity (see Figs. 4.16 and 4.17). Nevertheless CatI and CatII are combined for better statistics, leaving the possibility to treat them separately (see section 4.4.3).

The distribution of bubbles along the Galactic plane is shown on top of a H.E.S.S. significance map in Fig. 4.16. The radius and eccentricity distributions are shown in Figs. 4.17(c) and 4.17(d) respectively. The red and blue histograms show the distributions for CatI and CatII respectively.

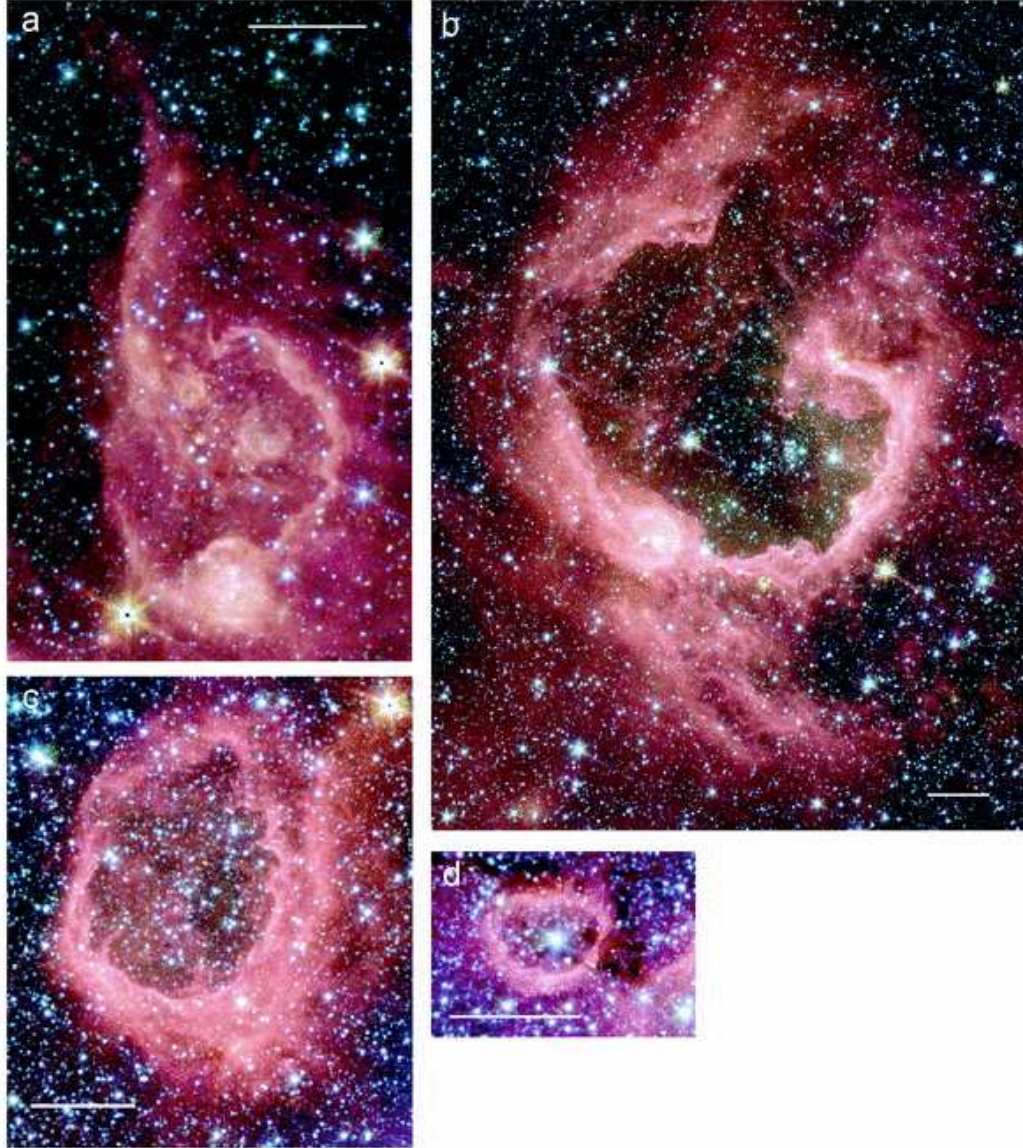


Figure 4.15: Bubbles seen in infrared (from Churchwell et al. 2006 [32]). The horizontal bar in each panel represents an angular size of $2'$. Different morphologies are shown (multiple bubble (a), broken and multiple bubble enclosing a star cluster (b), complete bubble (c), complete bubble with a central star (d)), but are not considered in the correlation study.

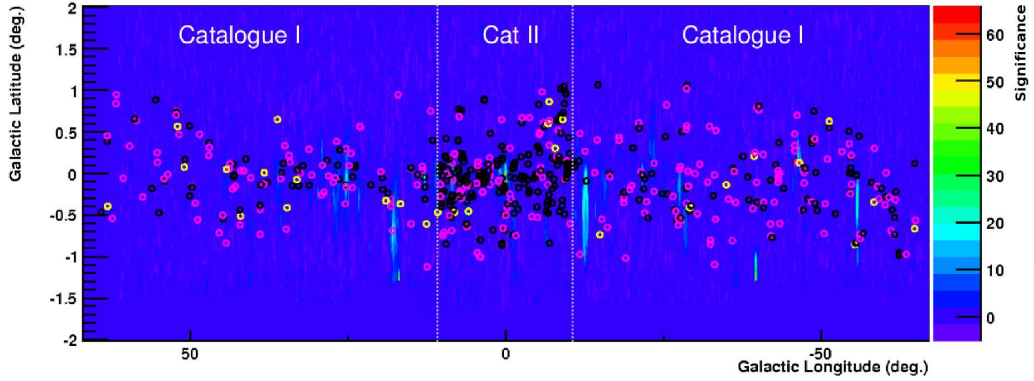


Figure 4.16: *H.E.S.S. significance map with the positions of bubbles (from [32] and [33]) superimposed. The circles are not to scale, however black circles represent bubbles with radii smaller than $1'$, pink circles and yellow circles represent bubbles with radii smaller or greater than $5'$ respectively. A clear difference in the density of (small) bubbles can be seen between the two catalogues.*

4.4.3 Monte-Carlo

For the Galactic bubbles, the only correlation between physical quantities found is between the latitude and the eccentricity. Therefore the eccentricity is used as the reference quantity for the Monte-Carlo. Since information about the bubble's size is given and because the IR emission comes from the rim of the bubbles, a significance map for point sources is searched for the maximal significance within the bubbles extend. Although the eccentricity and sometimes the length of the major and minor axis are given, the mean radius is used every time for the search, since the inclination angle is missing.

As mentioned before, the catalogue can be separated into a central and an outer Galactic region. Since it is difficult to fit a function to the histogram in Fig. 4.17(a), a random value for the longitude is directly picked from the histogram. Depending on the longitude the mean radius and eccentricity are picked from either a fit to the red or blue histograms in Figs. 4.17(c) and 4.17(d) respectively. The modelling of the eccentricity-latitude correlation however, is done with the data from the combined catalogues, since the distribution is very similar and because otherwise the statistics are very low.

4.4.4 Results

The results of the correlation study of Galactic bubbles with H.E.S.S. data are shown in Fig. 4.18. No correlation is found.

Neither the eccentricity nor the mean radius are promising quantities for finding any correlation. The surface brightness (as it was used for the SNRs and HII regions) could be an indication of the strength of the stellar wind. Nevertheless no

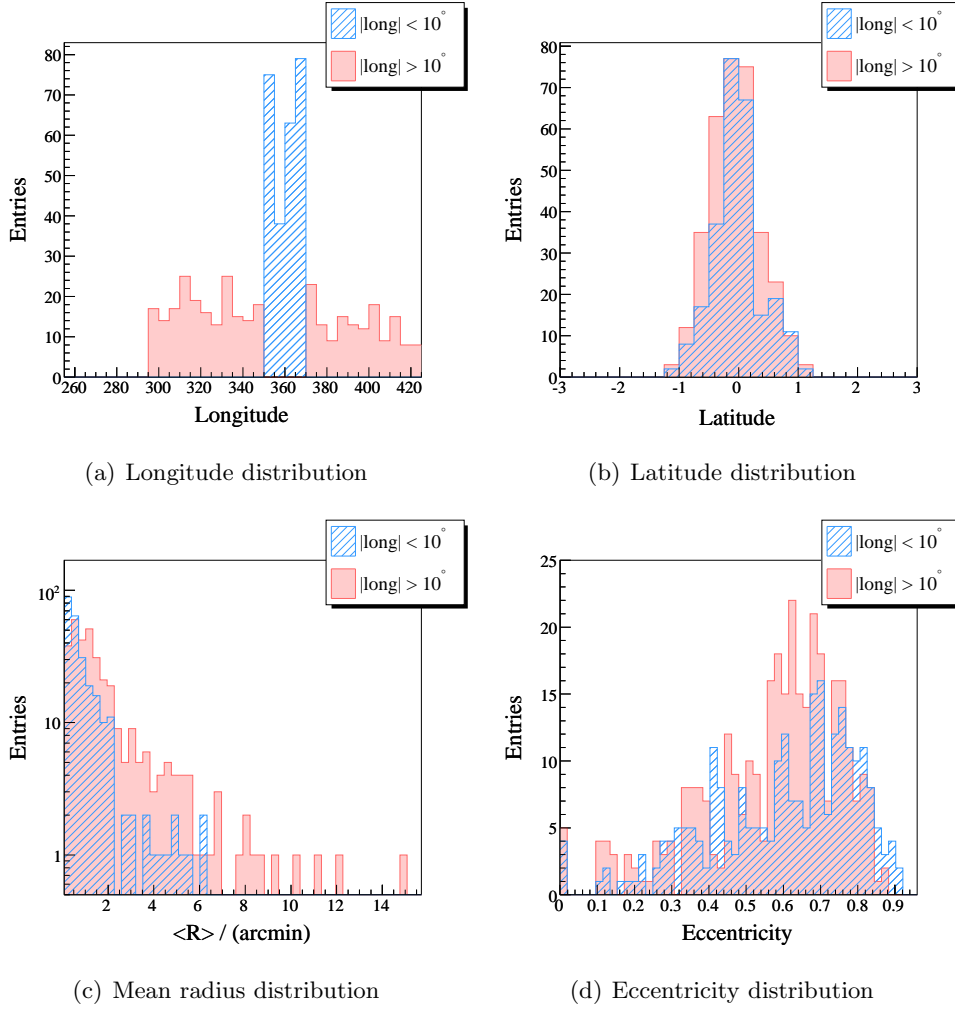


Figure 4.17: The distributions of the Galactic longitude, Galactic latitude, mean radius and eccentricity of the Galactic bubbles from [32] and [33]. The blue hashed histograms stand for the bubbles within $|l| < 10^\circ$, i.e. CatII, while the light red histograms represent the distributions of CatI, i.e. $|l| > 10^\circ$.

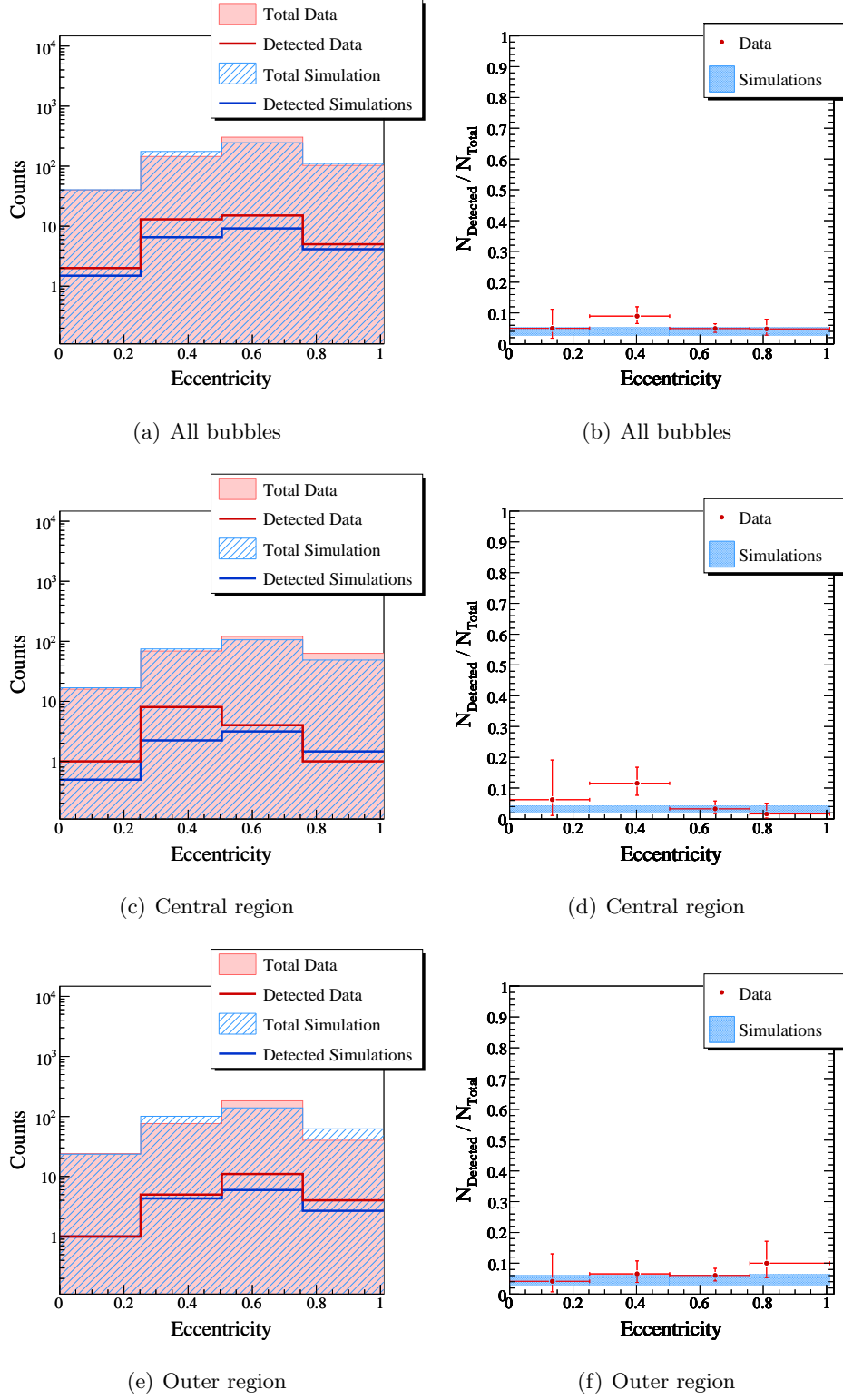


Figure 4.18: The results of the correlation study of the Galactic bubbles from [32] and [33] with H.E.S.S. data as a function of the eccentricity.

acceleration mechanisms are proposed for bubbles. In addition, neither the surface brightness, nor the flux density required to calculate the surface brightness are given in the catalogue.

4.5 OB stars and OB associations

OB stars are the hottest, and most massive stars of spectral types O or B (upper left in the Hertzsprung-Russel diagram, Fig. 4.19). They are born within giant molecular clouds and group into OB associations. During their relatively short lifetime, they emit significant amounts of ultraviolet radiation, ionising the surrounding interstellar gas of the giant molecular cloud and forming HII regions. Once the surrounding dust and gas is blown away, the remaining stars become unbound and begin to drift apart. Since the OB stars will have burned all their fuel within 10 million years, OB associations themselves are generally not older than a few million years. OB stars end their lives as supernovae of type Ib, Ic or type II. It is believed that the majority of all stars in the Milky Way were formed in OB associations.

4.5.1 Motivation

Due to the link between OB associations and star formation (see section 4.2), it is interesting to investigate if VHE γ -ray signals are emitted. In addition to possible VHE γ -rays related to star formation, there could be contributions from the interaction of the strong stellar winds with the interstellar medium (Völk and Forman [65]). In a different scenario, Torres et al. [62] propose that VHE γ -rays and neutrinos could be produced by cosmic rays through hadronic interactions in the innermost parts of the winds of massive OB stars. Lower Energy (MeV-GeV) γ -rays would be missing due to convection preventing low energy particles from entering the wind. They argue that groups of stars located close to the acceleration sites in OB associations may be detectable by ground based Cherenkov telescopes.

4.5.2 The catalogue

Massey et al. [51] provide a catalogue of OB associations in the northern Milky Way. Unfortunately, only two associations are within the H.E.S.S. scan region, making a correlation study quite useless. However, Reed [56] provides a catalogue of Galactic OB stars, with 18693 OB stars, 7528 of them being within the H.E.S.S. scan region. The catalogue contains different types of photometric data, of which the visual magnitude was used in this correlation study. This reduces the number of OB stars considered in this work to 5970.

4.5.3 Distributions and Monte-Carlo

The longitude, latitude and magnitude distributions of the 5970 OB stars used are shown in Fig. 4.20. The modelling of the OB stars does not differ from the basic method. The correlation between the latitude and the visual magnitude is

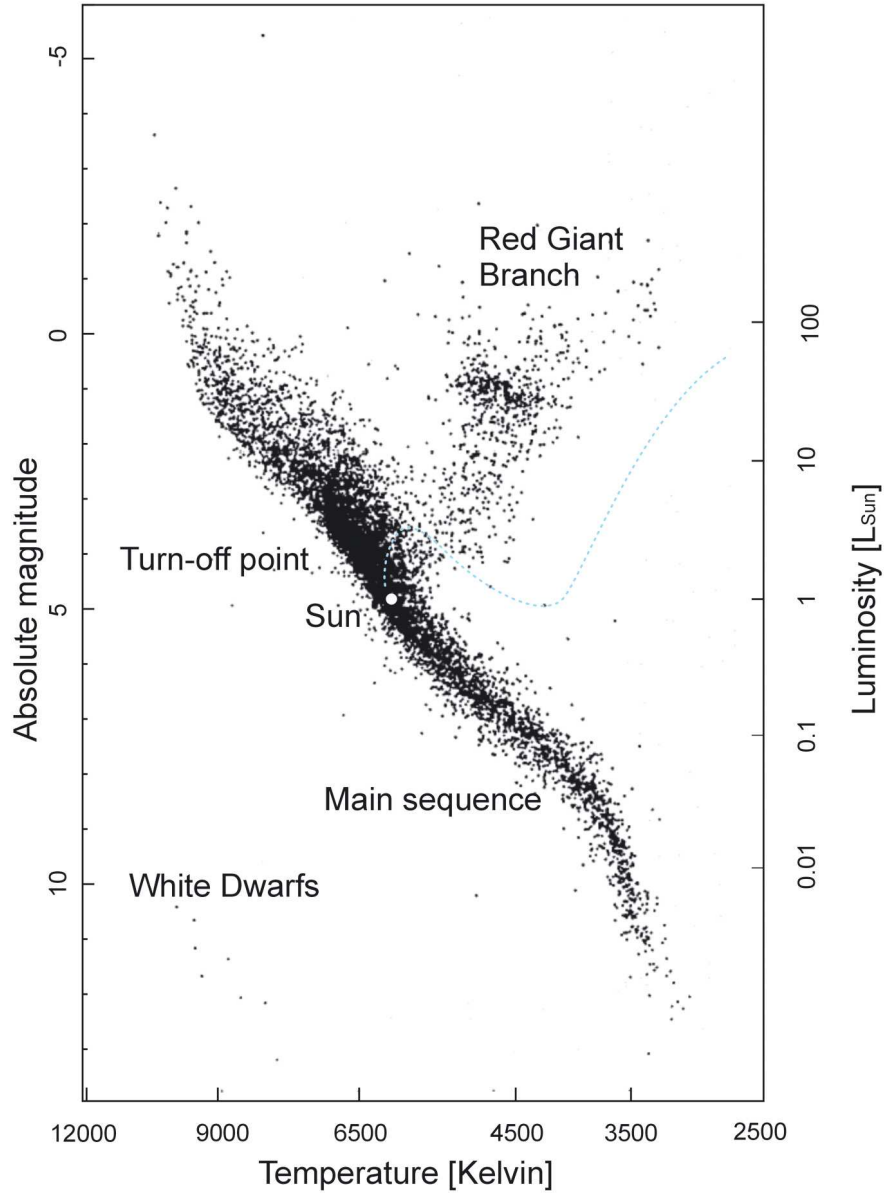


Figure 4.19: A Hertzsprung-Russell Diagram of nearby stars. The H-R diagram shows the relationship between surface temperature and luminosity of the stars. The position of a star on the diagram is determined by its surface temperature and its absolute magnitude. Note the prominent Main Sequence and the different regions where red giants and white dwarfs dominate. The location of the Sun is marked as well as the route that a star of one solar mass will follow during the different phases of its life. (Image from [3]).

modelled in exactly the same way as the energy flux density of the pulsars described in section 3.3.1.

4.5.4 Results

The results after $3 \cdot 10^4$ simulations are shown in Fig. 4.21. The corresponding probabilities of chance coincidences are listed in table 4.5. A significance map with a correlation radius of $\theta = 0.22^\circ$ was used in order to account for possible VHE γ -ray emission coming from colliding winds at some distance from the star. However, no correlation is found.

4.6 Wolf-Rayet stars

An intriguing class of astrophysical objects are the Wolf-Rayet stars (WR, see Fig. 4.6, left panel), named after their first observers Charles Wolf and George Rayet. Wolf-Rayet stars are very hot and massive stars which lose mass at a very high rate, due to their strong stellar winds with terminal velocities $v_\infty \sim 1000 - 5000$ km/s. These winds are driven by the radiation pressure of the WR-star. Although they are found close to the main sequence (upper left end) in the Hertzsprung-Russel diagram (Fig. 4.19), they are thought to be in the last phase of their life, after the Hydrogen-rich envelope has been blown away or transferred to a binary companion. The observational characteristics of WR stars are their broad and strong emission lines of Nitrogen, Carbon or Oxygen (also called WN, WC or WO stars, respectively). These emission lines are formed in the extended envelope of the stars, where the high velocity winds are responsible for the fluorescence of the elements. Wolf-Rayet stars are believed to explode as supernovae of type Ib or Ic.

4.6.1 Motivation

The strong stellar winds, which can possibly accelerate particles up to relativistic energies, as well as the fact that at least 40-50% of Wolf-Rayet stars are found in binaries, where stellar winds collide, make the WR stars interesting for γ -ray astronomy. This is supported by the observation of non-thermal radio emission (e.g. Abbott et al. [7]), which have been interpreted by synchrotron emission. Several acceleration sites are proposed, either in shocks caused by the instability of radiatively driven winds (White [67]), in the shocked winds collision region of multiple systems or in the terminal shock (e.g. Völk and Forman [65]).

It is now assumed that γ -ray emission should also be expected, either through leptonic processes, i.e. inverse Compton scattering of the UV photons and relativistic bremsstrahlung or via hadronic interactions of co-accelerated ions with the dense wind material (see [57] and references therein). The positional coincidences of WR-binary systems with the population of unidentified EGRET sources might support these assumptions, however no individual WR binary systems could be identified as a high energy γ -ray emitter with EGRET. The link between non-thermal radio

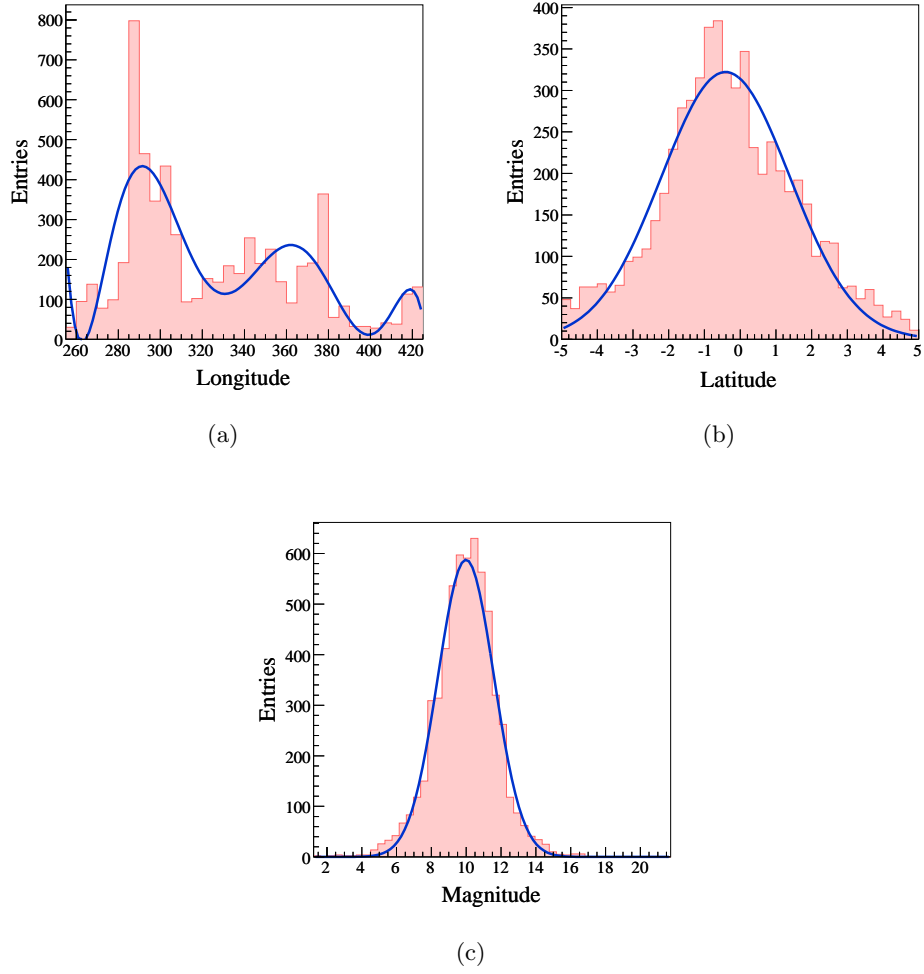


Figure 4.20: *The distributions of the Galactic longitude, Galactic latitude and visual magnitude of the OB stars from [56] within the H.E.S.S. scan region.*

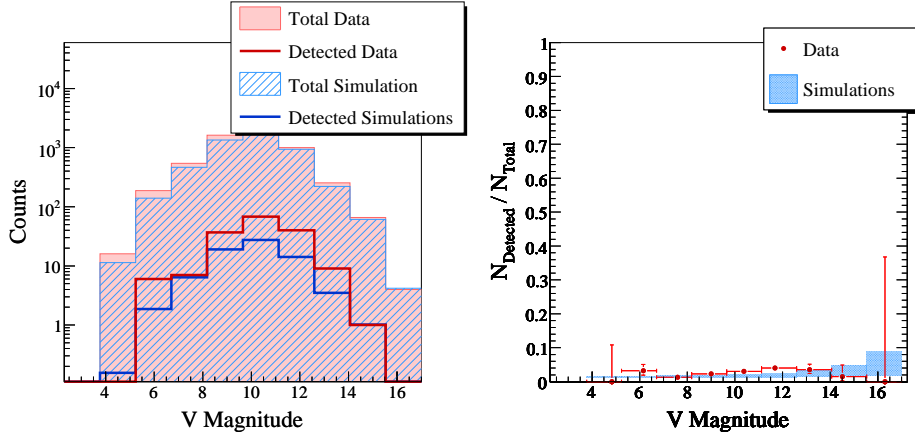


Figure 4.21: The results of the correlation study of the OB stars from [56] with *H.E.S.S.* data. **Left** Distribution of all (filled areas) and detected (lines) OBSs for the data (red) and the simulation (blue) as a function of the visual magnitude, for all the OB stars within the *H.E.S.S.* scan region. **Right** Ratio of detected over all OB stars for the data (red) and simulations (blue) as a function of the visual magnitude. See text for a discussion of these results.

visual magnitude $\log[F_{2.7\text{GHz}}/\text{Jy}]$	Detections out of #OB stars	Probability of chance coincidence
3.8 - 5.2	≥ 0 out of 16	99.3%
5.2 - 6.7	≥ 6 out of 187	8.00%
6.7 - 8.2	≥ 7 out of 543	73.4%
8.2 - 9.7	≥ 37 out of 1629	8.66%
9.7 - 11.1	≥ 68 out of 2223	0.051%
11.1 - 12.6	≥ 40 out of 1000	0.14%
12.6 - 14.0	≥ 9 out of 254	38.2%
14.0 - 15.5	≥ 1 out of 66	78.2%
15.5 - 17.0	≥ 0 out of 17	78.0%

Table 4.5: The probabilities of chance coincidences for OB stars from [56] with *VHE* γ -ray signals. See text for a discussion of these results.

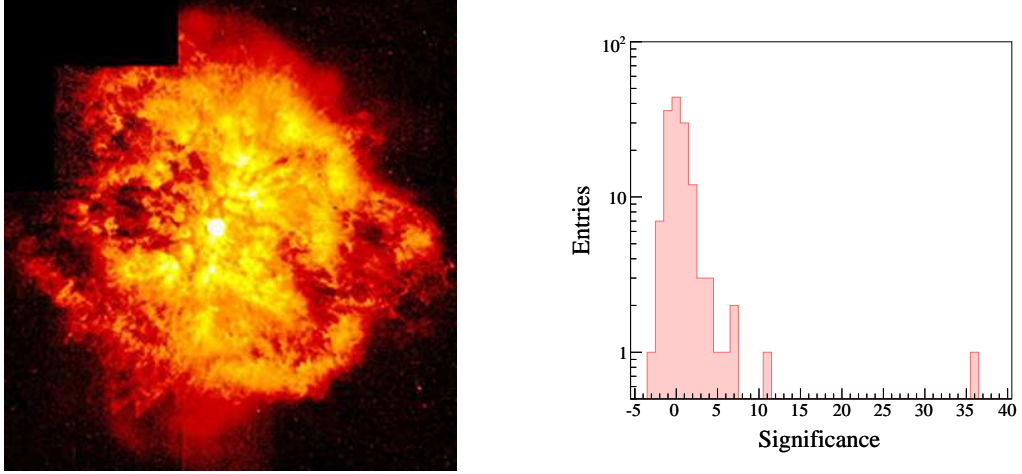


Figure 4.22: **Left:** The Wolf-Rayet star WR 124 and its surrounding nebula in the constellation Sagittarius as observed with the Hubble Space Telescope. (Image from [6]). **Right:** The distribution of the significance in a H.E.S.S. significance map with $\theta = 0.22$ for the Wolf-Rayet stars from [63], [64].

long	lat	sign	H.E.S.S.	Counterpart
320.26	-1.20	35.66	J1514-591	MSH 15-5 2
368.29	-0.16	11.03	J1804-216	G8.7-0.1 / W30?; PSR J1803-2137?
320.55	-1.19	6.77	J1514-591	MSH 15-5 2
284.33	-0.35	6.56	J1023-575	WR 20a; Westerlund 2; RCW 49
377.54	-0.13	6.16	J1825-137	PSR J1826-1334; 3EG J1826-1302 ?
284.27	-0.34	4.96	J1023-575	WR 20a; Westerlund 2; RCW 49
376.98	-1.03	4.29	J1826-148	LS 5039
292.09	-0.54	3.84	J1119-614	
366.44	-0.49	3.62	J1804-216	G8.7-0.1 / W30?; PSR J1803-2137?

Table 4.6: **Right:** The Wolf-Rayet stars from [64] with the highest significance, the corresponding H.E.S.S. source and the know counterparts of the H.E.S.S. sources.

emission and the binarity of stellar systems (Dougherty and Williams [21]) supports the scenario in which particles are predominantly being accelerated at the forward and reverse shocks from colliding supersonic winds of massive stars. Since a considerable proportion of WR stars is found in binary systems, the emission of γ -rays originating in the collision of stellar winds can be expected (see Reimer et al. [57]).

4.6.2 The catalogue and statistics

The VIIth Catalogue of Galactic Wolf-Rayet stars and its annex presented by van der Hucht [63], [64] contain 298 Wolf-Rayet stars. About 80% of them are embedded in HII regions, while 46% are found in open clusters or OB associations. The Catalogue gives information about the locations of the WR stars, their environment, their photometric distances and some of their parameters like the terminal wind velocity, spectral information and the periodicity (if available).

When superimposing the positions of known WR stars on a H.E.S.S. significance map ($\theta = 0.22^\circ$) and counting the detected WR stars, one can see that a further correlation study is superfluous (see Fig. 4.22, right panel, and table 4.6). Only five WR stars are found with a significance above 5σ and what is more, all of these VHE γ -ray sources have known counterparts. Even if a lower detection criteria of 3 or 4σ is used, a correlation study would be quite useless so far, since the signals from these “detected” WR stars come from H.E.S.S. sources with usually known counterparts (table 4.6, lower part). Since for the special case WR140, Reimer et al. [57] predict a photon spectrum ranging up to $\sim 10 - 100$ GeV, which would only allow low energy threshold IACTs to detect it, the missing detections are comprehensible. However, since the number of known Galactic WR stars is constantly increasing ($\sim 30\%$ between 2001 and 2006) and with the improved sensibility of the upcoming H.E.S.S. II telescope, the available statistics may very well increase such that a correlation study may be of more importance soon.

4.7 X-ray binaries

Many stars are, unlike the Sun, found in binary star systems, where two stars rotate about the centre of mass of the system. When matter from one (usually normal) star flows onto a compact binary companion (i.e. neutron star or a black hole) X-rays are produced. Such binaries are called X-ray binaries. The emitted X-rays come from the gravitational potential energy released when the matter falls onto the compact star. Generally an accretion disc forms around the compact objects and in some cases two jets leave the compact star at its poles (see Fig. 4.23). X-ray binaries with jets are called micro-quasars.

The X-ray binaries can be subdivided into low-mass X-ray binaries (LMXBs) and high-mass X-ray binaries (HMXBs). In LMXBs the donor star is usually less massive than the compact object. The donor star can be on the main sequence (see Fig 4.19) or an evolved star (red giant). The mass transfer is via Roche-Lobe overflow, i.e. the stellar matter leaves the region in which it is gravitationally bound

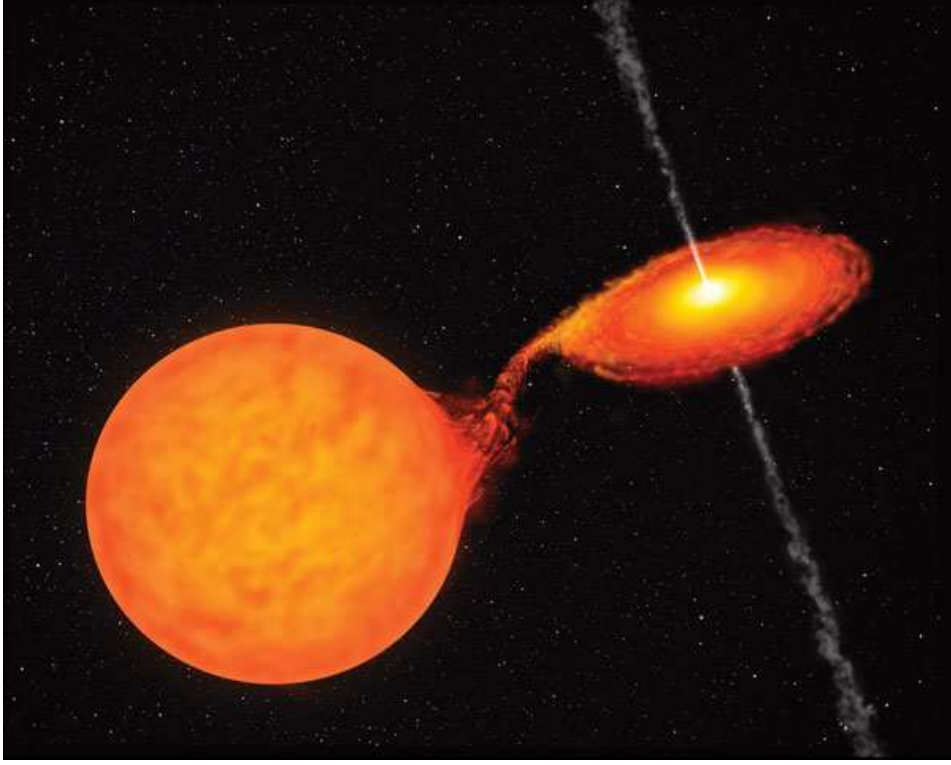


Figure 4.23: *An artist's impression of an X-ray binary. The mass overflow and two jets coming from the compact object are shown. (Image from [23])*

to the donor star and enters the gravitational region of the compact companion. HMXBs are binary star systems in which the normal stellar component is a massive star, usually an O or B star, a Be star or a blue supergiant. In HMXBs the mass transfer can occur via Roche-lobe overflow or strong stellar winds.

4.7.1 Motivation

Four high-mass X-ray binaries, but no LMXB, have already been detected in VHE γ -rays (see Paredes [55]). The observational results on those sources show that very effective particle acceleration takes place, since Photons have been observed up to 30 TeV. In the case of the detected HMXB Cygnus X-1, the compact object is an accreting black hole, while for PSR B1259-63, which is also detected in VHE γ -rays, the compact object is a non-accreting neutron star. The nature of the other two detected HMXBs is as yet unknown. Only PSR B1259-63 and LS 5039 are within the H.E.S.S. scan region.

The proposed scenarios for VHE γ -ray production in micro-quasars (i.e. XRB with jets) include inverse Compton up-scattering of stellar UV photons from the companion star by the relativistic electrons in the jet (see e.g. Paredes et al. [54]) or

hadronic processes either within the jet or in the interaction between the relativistic jets and the interstellar medium (Romero et al. [58]). It has also been proposed that VHE γ -ray could be produced by the interaction of the stellar wind of a young non-accreting neutron star and its companion's stellar wind [22].

4.7.2 The catalogue

Liu et al. [48] provide a catalogue of HMXB which is used in this correlation study. The catalogue contains 114 HMXB of which 75 are within the H.E.S.S. scan region. It gives information about the source name(s), coordinates, finding chart, X-ray luminosity, system parameters, and stellar parameters of the components and other characteristic properties of the HMXB, together with a comprehensive selection of the relevant literature. In this work, only the flux in the range 2 - 20 keV was used as a relevant parameter. Unfortunately, a value for the flux in that range is only given for 83 binaries. About 60% of the high-mass X-ray binary candidates are known or suspected Be/X-ray binaries, while 32% are supergiant/X-ray binaries. Some sources, however, are only tentatively identified as HMXBs on the basis of their X-ray properties similar to the known HMXBs. Further identification in other wavelength bands is needed to finally determine the nature of these sources.

4.7.3 Monte-Carlo

The distributions relevant for the Monte-Carlo are shown in Fig. 4.24. Since no size can be given and only one parameter - the flux in the range 2 - 20 keV - is used, the Monte-Carlo is done following the basic method as for the PWNe. However, since no correlation is found between the flux and the latitude (maybe due to low statistics), the latitude is modelled from its distribution (Fig. 4.24(b)) rather than from flux bands as in the basic method.

4.7.4 Results

Figure 4.25 shows HMXBs which are detected with H.E.S.S. in a significance map for point-like sources (i.e. $\theta = 0.1^\circ$). The probabilities of chance coincidence are summarised in table 4.7. The results are rather inconclusive, which is mainly due to the low statistics. HMXB are able to emit VHE γ -rays since four of them have been detected, however the nature of these HMXBs and the conditions for the detection remain unclear.

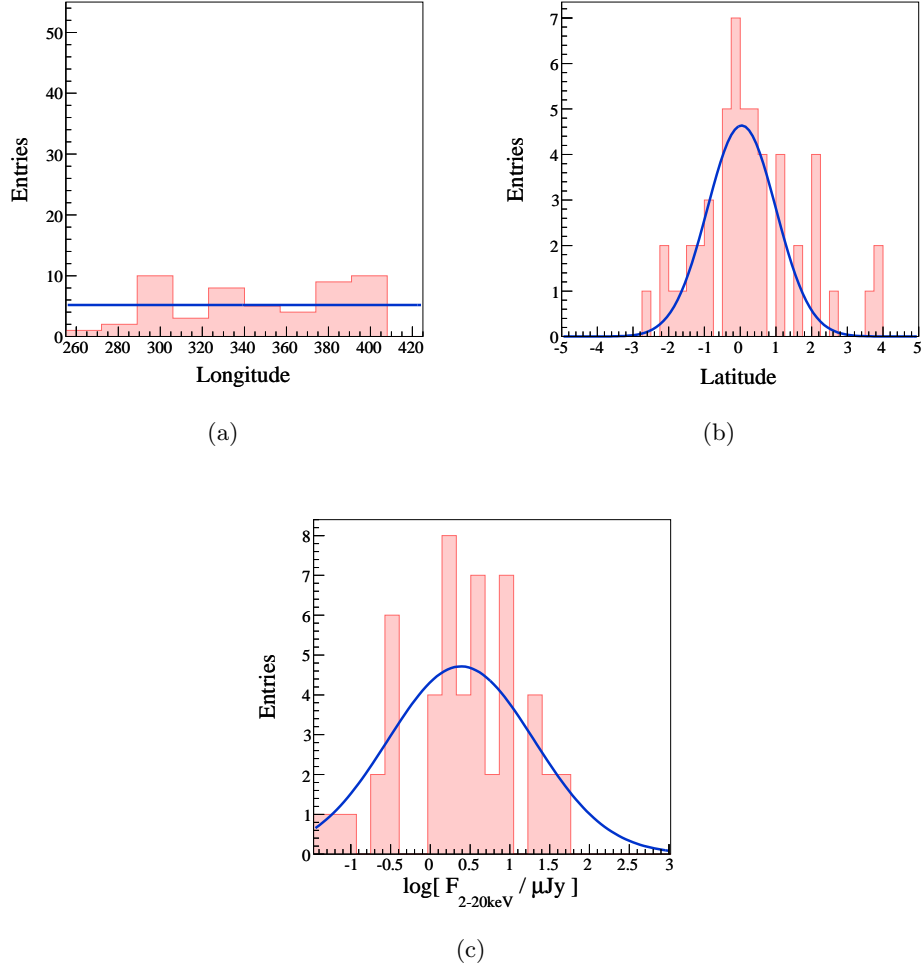


Figure 4.24: The distributions of the Galactic longitude, Galactic latitude and flux of the high mass X-ray binaries from [48].

Flux $\log[F_{2-20\text{keV}} / \mu\text{Jy}]$	Detections out of #HMXBs	Probability of chance coincidence
0.1 - 1.6	≥ 3 out of 36	1.14%

Table 4.7: The probabilities of chance coincidences for HMXBs from [48] with VHE γ -ray signals. See text for a discussion of these results.

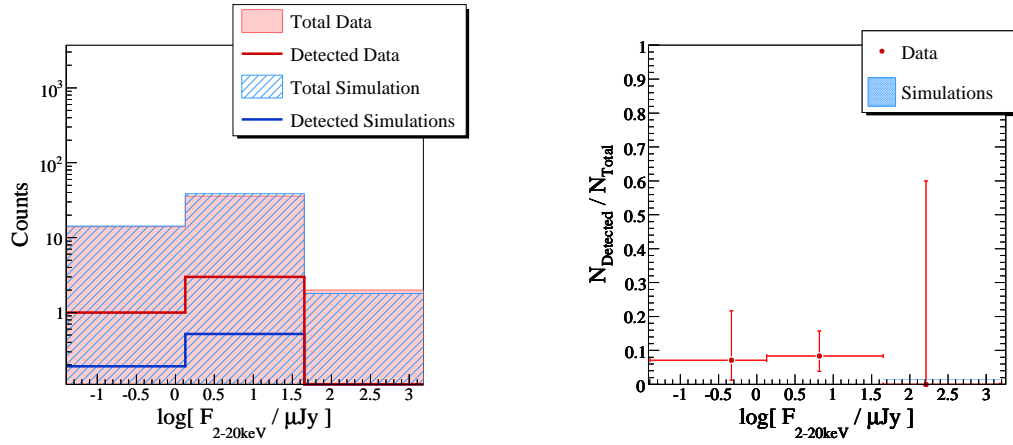


Figure 4.25: The results of the correlation study of the HMXBs from [48] with *H.E.S.S.* data as a function of the flux in the range 2 - 20 keV. **Left:** Distribution of all (filled) and detected (line) HMXBs for the data (red) and the simulation (blue) as a function of the flux in the range 2 - 20 keV, for the HMXBs within the *H.E.S.S.* scan region. **Right:** Ratio of detected over all HMXBs for the data (red) and simulations (blue) as a function of the flux in the range 2 - 20 keV, for all the HMXBs within the *H.E.S.S.* scan region.

Chapter 5

Summary and outlook

In this work, a general tool has been developed, which performs statistical correlation studies between Galactic objects and VHE γ -ray sources. The method is based on the work by Carrigan [16], in which such a correlation study is applied on pulsar wind nebulae. As opposed to [16], where the PWNe are known possible γ -ray emitters and some insight on the production of VHE γ -rays of PWNe is searched, this work concentrates on finding correlations between the astrophysical objects and VHE γ -ray sources, without necessary being the source of the VHE γ -rays. This is reasonable since a considerable amount of H.E.S.S. sources do not have any counterpart determined with certainty yet. A positive correlation of astrophysical objects with VHE γ -rays does not imply that the objects in question emit the VHE γ -rays themselves. Some mechanisms related to the objects or their environment could be responsible for VHE γ -ray emission, for example if investigating the VHE γ -ray emission within HII or star forming regions, objects within these region might be the source of the emission, or vice-versa when investigating objects within those regions.

Brief conclusions on the correlation studies of all objects performed in this work are summarised in table 5.1. HII regions [36], Galactic bubbles [32], [33] and OB stars [56] do not show significant correlations with VHE γ -rays. Note that these three types of objects are related (OB stars ionise HII regions and can form bubbles, sometimes within HII regions) so that the results can be considered consistent. Although several scenarios for VHE γ -ray emission are proposed for Wolf-Rayet stars [63] due to their strong stellar winds, the amount of known WR stars coinciding with H.E.S.S. sources is too limited for a meaningful correlation study. Maybe in the future, with more known WR stars and telescopes with better sensitivity a correlation study can be performed. Four high mass X-ray binaries [48] are known to emit VHE γ -rays, but unfortunately the limited number of HMXBs known in our Galaxy does not allow the investigation of trends dependent on physical quantities of the binaries.

Star forming complexes [59] and regions of star formation [10] both seem to correlate with VHE γ -ray emission. For star forming complexes the rate of detections seems to increase with higher excitation parameter, but the statistics are too low for decisive conclusions. Furthermore, the uncertainty in the excitation parameter could

OBJECTS	CONCLUSIONS
Supernova remnants [43]	The rate of detections seems to increase with higher surface brightness, but the statistics are limited. Single VHE γ -ray sources with SNR counterparts were already known.
Star forming complexes [59]	The rate of detections seems to increase with higher excitation parameter, however the statistics are too low for decisive conclusions.
Regions of star formation [10]	The rate of detections is significant only for one class of RSF, however clumping and multiple RSF on H.E.S.S. sources could have affected the probabilities of chance coincidence. Furthermore, missing information and homogeneity in the catalogue makes Monte-Carlo simulations difficult.
HII regions [36]	HII regions do not seem to correlate significantly with VHE γ -rays.
Galactic bubbles [32], [33]	Galactic bubbles do not correlate with VHE γ -rays.
OB stars [56]	OB stars do not seem to correlate significantly with VHE γ -rays.
Wolf-Rayet stars [63]	The statistics of detected WR stars from the data is too low for a meaningful correlation study.
High mass X-ray binaries [48]	Some HMXB can be detected in VHE γ -rays, since four HMXB have been identified as the counterparts of VHE γ -ray sources. However, for this correlations study the statistics of the catalogue are too low for the identification of any trend.

Table 5.1: *Brief conclusions on the correlations studies performed in this work.*

have slightly affected the results. From the regions of star formation [10], only one class seems to correlate with VHE γ -rays, i.e. those where it is supposed that massive stars are formed and where the missing optical data suggest large distances. It could be worth to investigate this catalogue somewhat further. An enormous amount of data is available, but it needs to be sorted and a synthetic catalogue, like the HII regions catalogue [36], where the flux is determined for one frequency for all objects would make a meaningful Monte-Carlo simulation possible. However, the size of the majority of the RSF - an important information - would still be missing.

Supernova remnants are known γ -ray emitters, however the predicted amount of such SNRs has not been detected yet. Although from the correlations study in this work it seems that SNRs with higher surface brightness are more likely to emit VHE γ -rays, their number and the statistics remain rather low for decisive conclusions. This is even more the case, when the shell type SNRs are separated from all SNRs (including SNRs with PWNe). This might be due to the contribution of possibly detected PWNe, but can also reflect the lower statistics.

The generalised tool for correlation studies between astrophysical objects and H.E.S.S. data has proven to be useful in a first estimation of possible relations between astrophysical objects and VHE γ -rays. However, the results often remain inconclusive, which is strongly due to the generally low statistics available from the catalogues. In the future, as the sensitivity of telescopes will surely increase - including H.E.S.S. with phase II - more (precise) data on both astrophysical objects and VHE γ -rays will become available, increasing the statistics. At this point, the correlation studies performed in this work can be repeated. Furthermore, there are available catalogues in the literature which have not been considered in this work. The general tool developed in this work can be applied on those catalogues and maybe provide some new insight.

Bibliography

- [1] https://www.mpi-hd.mpg.de/hfm/hess/intern/wiki/the_h.e.s.s._source_catalog.
- [2] <http://heasarc.gsfc.nasa.gov/>.
- [3] <http://www.astroex.org/english/exercise4/images.php>.
- [4] <http://wwwmagic.mppmu.mpg.de/>.
- [5] <http://veritas.sao.arizona.edu/content/blogsection/6/40/>.
- [6] http://nssdc.gsfc.nasa.gov/photo_gallery/photogallery-astro-exotic.html.
- [7] D. C. Abbott, J. H. Beiging, E. Churchwell, and A. V. Torres. Radio emission from galactic Wolf-Rayet stars and the structure of Wolf-Rayet winds. *ApJ*, 303:239–261, 1986.
- [8] F.A. Aharonian. *Very high energy cosmic gamma radiation: a crucial window on the extreme Universe*. River Edge, NJ: World Scientific Publishing, 2004.
- [9] A. T. Araudo, G. E. Romero, V. Bosch-Ramon, and J. M. Paredes. Gamma-ray emission from massive young stellar objects. *A&A*, 476:1289–1295, 2007.
- [10] V.S. Avedisova. A Catalog of Star-Forming Regions in the Galaxy. *Astronomy Reports*, 46(3):193–205, 2002.
- [11] K. Belotsky. Correlation between regions of star formation and gamma-ray sources. *Bulletin of the Russian Academy of Sciences: Physics*, 71:915–917, 2007.
- [12] D. Berge, S. Funk, and J. Hinton. Background Modelling in Very-High-Energy γ -rays Astronomy. *A&A*, 466:1219–1229, 2007.
- [13] K. Bernlöhner. <http://www.mpi-hd.mpg.de/hfm/bernlöhner/HESS/>.
- [14] F. Bocchino and R. Bandiera. BeppoSAX observation of the composite remnant G327.1-1.1. *A&A*, 398:195–202, 2003.

BIBLIOGRAPHY

- [15] O. Bolz. *Absolute Energiekalibration der abbildenden Cherenkov-Teleskope des H.E.S.S. Experiments und Ergebnisse erster Beobachtungen des Supernova-Überrests RX J1713.7-3946*. PhD thesis, Ruperto-Carola University of Heidelberg, 2004.
- [16] S. Carrigan. *Pulsar Wind Nebulae with H.E.S.S.: Establishing a Connection between high-power Pulsars and very-high-energy gamma-ray Sources*. PhD thesis, Ruperto-Carola University of Heidelberg, 2007.
- [17] C. J. Clopper and E. S. Perason. The use of the confidence or fiducial limits illustrated in the case of the binomial. *Biometrika*, 26:404, 1934.
- [18] The Pierre Auger Collaboration and J. Abraham et al. Correlation of the Highest-Energy Cosmic Rays with Nearby Extragalactic Objects. *Science*, 318: 938, 2007.
- [19] J. Cronin, T.K. Gaisser, and S.P. Swordy. Cosmic rays at the energy frontier. *Sci. Amer.*, 276:44, 1997.
- [20] J. M. Davies and E. S. Cotton. Design of the quartermaster solar furnace. *Journal of Solar Energy*, 1:16–22, 1957.
- [21] S. M. Dougherty and P. M. Williams. Non-thermal emission in Wolf-Rayet stars: are massive companions required? *MNRAS*, 319:1005–1010, 2000.
- [22] G. Dubus. Gamma-ray binaries: pulsars in disguise? *A&A*, 456:801–817, 2006.
- [23] A. Eckart. Astronomy: X-rays reveal the Galaxy’s centre. *Nature*, 415:129–129, 2002.
- [24] T. Eiffert. *Search for Pulsed Very High Energy Gamma Ray Emission from the Millisecond Pulsar PSR J0437-4715 with H.E.S.S.* Diploma thesis, Humboldt University Berlin, 2005.
- [25] Aharonian et al. Evidence for TeV gamma ray emission from Cassiopeia A. *A&A*, 370:112, 2001.
- [26] Aharonian et al. Calibration of cameras of the H.E.S.S. detector. *Astroparticle Physics*, 22:109–125, 2004.
- [27] Aharonian et al. A New Population of Very High Energy Gamma-Ray Sources in the Milky Way. *Science*, 307:1938–1942, 2005.
- [28] Aharonian et al. Observations of the Crab nebula with H.E.S.S. *A&A*, 457: 899–915, 2006.
- [29] Aharonian et al. The H.E.S.S. Survey of the Inner Galaxy in Very High Energy Gamma Rays. *ApJ*, 636:777–797, 2006.

- [30] Benjamin et al. GLIMPSE. I. An SIRTf Legacy Project to Map the Inner Galaxy. *PASP*, 115:953–964, 2003.
- [31] Buckley et al. Constraints on cosmic-ray origin from TeV gamma-ray observations of supernova remnants. *A&A*, 329:639–658, 1998.
- [32] Churchwell et al. The bubbling Galactic disk. *ApJ*, 649:759, 2006.
- [33] Churchwell et al. The bubbling Galactic disk. II. The inner 20°. *ApJ*, 670:428, 2007.
- [34] Enomoto et al. The acceleration of cosmic-ray protons in the supernova remnant RX J1713.7-3946. *Nature*, 416:823–826, 2002.
- [35] Hobbs et al. The Parkes multibeam pulsar survey - IV. Discovery of 180 pulsars and parameters for 281 previously known pulsars. *MNRAS*, 352:1439, 2004.
- [36] Paladini et al. A radio catalog of Galactic HII regions for applications from decimeter to millimeter wavelengths. *A&A*, 397:213, 2003.
- [37] Weekes et al. Observation of TeV gamma rays from the Crab nebula using the atmospheric Cerenkov imaging technique. *ApJ*, 342:379–395, 1989.
- [38] E. Fermi. On the Origin of the Cosmic Radiation. *Phys. Rev.*, 75:1169 – 1174, 1949.
- [39] S. Funk. *A new population of very high-energy gamma-ray sources detected with H.E.S.S. in the inner part of the Milky Way*. PhD thesis, Ruperto-Carola University of Heidelberg, 2005.
- [40] M. Füssling. *Study of an Observation Mode with Convergent Pointing and a Topological Trigger for the H.E.S.S. Experiment*. Diploma thesis, Humboldt University Berlin, 2006.
- [41] V. L. Ginzburg and S. I. Syrovatskii. *The Origin of Cosmic Rays*. Macmillan, New York, 1964.
- [42] D.A. Green. Galactic supernova remnants: an updated catalogue and some statistics. *Bull. Astr.Soc. India*, 32:335–370, 2004.
- [43] D.A. Green. A Catalogue of Galactic Supernova Remnants (2006 April version). *Astrophysics Group, Cavendish Laboratory, Cambridge, United Kingdom (available at <http://www.mrao.cam.ac.uk/surveys/snrs/>)*, 2006.
- [44] W. Heitler. *Quantum Theory of Radiation*. Dover Press, 1954.
- [45] A. M. Hillas. Topical review: Can diffusive shock acceleration in supernova remnants account for high-energy galactic cosmic rays? *Journal of Physics G Nuclear Physics*, 31:95, 2005.

BIBLIOGRAPHY

- [46] A. M. Hillas. Cerenkov light images of EAS produced by primary gamma. *Proc. 19th ICRC*, pages 445–448, 1985.
- [47] T.P. Li and Y.-Q. Ma. Analysis methods for results in gamma-ray astronomy. *ApJ*, 272:317, 1983.
- [48] Q.Z. Liu, J. van Paradijs, and E.P.J. van den Heuvel. Catalogue of high-mass X-ray binaries in the Galaxy (4th edition). *A&A*, 455:1165–1168, 2006.
- [49] F. J. Lockman, D. J. Pisano, and G. J. Howard. Detection of 130 Diffuse Galactic HII Regions. *ApJ*, 472:173, 1996.
- [50] M. S. Longair. *High Energy Astrophysics Volume 2: Stars, the Galaxy and the interstellar medium*. Cambridge University Press, 1994.
- [51] P. Massey, K. E. Johnson, and K. Degioia-Eastwood. The Initial Mass Function and Massive Star Evolution in the OB Associations of the Northern Milky Way. *ApJ*, 454:151, 1995.
- [52] T. Montmerle and C. J. Cesarsky. Cosmic-ray confinement by resonant Alfvén waves and gamma-ray emission in HII regions. *ICRC*, 1:173, 1981.
- [53] NASA, ESA, T. Megeath (University of Toledo), and M. Robberto (STScI). <http://hubblesite.org/newscenter/archive/releases/2006/01/image/q/>.
- [54] J. M. Paredes, V. Bosch-Ramon, and G. E. Romero. Spectral energy distribution of the γ -ray microquasar LS 5039. *A&A*, 451:259–266, 2006.
- [55] J.M. Paredes. VHE Gamma-rays from Galactic X-ray Binary Systems. *ArXiv e-prints*, 2008.
- [56] C. Reed. Photometry and Spectroscopy for Luminous Stars. *Astron. J.*, 130:1652, 2005.
- [57] A. Reimer, O. Reimer, and M. Pohl. Gamma rays from colliding winds of massive stars. *Astrophys Space Sci*, 309:351–357, 2007.
- [58] G. E. Romero, H. R. Christiansen, and M. Orellana. Hadronic High-Energy Gamma-Ray Emission from the Microquasar LS I +61 303. *ApJ*, 632:1093–1098, 2005.
- [59] D. Russeil. Star-forming complexes and the spiral structure of our Galaxy. *A&A*, 397:133–146, 2003.
- [60] J. Schraml and P. G. Mezger. Galactic H II Regions.IV. 1.95-CM Observations with High Angular Resolution and High Positional Accuracy. *ApJ*, 156:269–302, 1969.
- [61] M. Sun, Z.-R. Wang, and Y. Chen. X-Ray Observation and Analysis of the Composite Supernova Remnant G327.1-1.1. *ApJ*, 511:274–281, 1999.

- [62] D.F. Torres, E. Domingo-Santamaria, and G.E. Romero. High-Energy gamma rays from stellar associations. *ApJ*, 601:75–78, 2004.
- [63] K.A. van der Hucht. The VIIth catalogue of Galactic Wolf-Rayet stars. *New Astronomy Reviews*, 45:135–232, 2001.
- [64] K.A. van der Hucht. New Galactic Wolf-Rayet stars, and candidates (Research Note) - An annex to the VIIth catalogue of Galactic Wolf-Rayet stars. *A&A*, 458:453–459, 2006.
- [65] H. J. Völk and M. Forman. Cosmic rays and gamma-rays from OB stars. *ApJ*, 253:188–198, 1982.
- [66] T. Weekes. *Very High Energy Gamma-Ray Astronomy*. Institute of Physics Publishing, 2003.
- [67] R. L. White. Synchrotron emission from chaotic stellar winds. *ApJ*, 289:698–708, 1985.

BIBLIOGRAPHY

Acknowledgements

An dieser Stelle möchte ich mich bei allen bedanken, die auf unterschiedlichster Art und Weise zum Gelingen dieser Arbeit beigetragen haben. Mein besonderer Dank gilt:

- meinem Betreuer Andreas Förster, dafür dass ich Dich jederzeit von Deiner Arbeit ablenken durfte, um Fragen zu stellen, für die viele nützlichen Kommentare und interessanten Gespräche sowie für das Korrekturlesen dieser Arbeit,
- Professor Werner Hofmann, für die Möglichkeit eine besonders interessante Diplomarbeit durchführen zu dürfen,
- Wilfried Domainko, für die Geduld, bei jedem Besuch in Eurem Büro, die Antworten auf meine astronomischen Fragen, das Korrekturlesen dieser Arbeit und die regelmäßige Erinnerung an den Preis eines gewissen Getränks in einer gewissen Straße,
- der gesamten H.E.S.S. Arbeitsgruppe für die angenehme Arbeitsatmosphäre und die Hilfe bei kleinen Problemen jeder Art,
- Tobias Herr und Steven Ehlert für die schönen Spaziergänge und interessanten Gespräche,
- Susanne und Anja für all den Stress, den wir uns neben dem Studium gemacht haben und sich trotz allem gelohnt hat, und für eure Freundschaft,
- Raphael für das Korrekturlesen sowie all meinen Freunden, für die vielen schönen Momente in den letzten 3 (minus 1) Jahren in Heidelberg, und ganz besonders Daniel, dafür dass wir nach all der Zeit doch noch zu einander gefunden haben und dass Du für mich da bist.

Schließlich möchte ich meinen Eltern, Elisabeth und Fritz-Harald sowie meiner Schwester Sabrina danken, für die Unterstützung und die Geduld in all meinen Unternehmungen und Lebensphasen.

Erklärung

Ich versichere, dass ich diese Arbeit selbständig verfasst und keine anderen als die angegebenen Quellen und Hilfsmittel benutzt habe.

Heidelberg, den _____

(Isabelle Wenig)